DEKAF

Spectral multi-regime basic-state solver for boundary-layer stability

Groot, Koen J.; Miró Miró, Fernando; Beyak, Ethan S.; Moyes, Alexander J.; Pinna, Fabio; Reed, Helen L.

DOI
10.2514/6.2018-3380

Publication date
2018

Document Version
Accepted author manuscript

Published in
2018 Fluid Dynamics Conference

DEKAF: Spectral Multi-Regime Basic-State Solver for Boundary-Layer Stability

Koen J. Groot,*Fernando Miró Miró,†Ethan S. Beyak,‡
Alexander J. Moyes,‡Fabio Pinna,§Helen L. Reed¶
*Delft University of Technology, Delft, 2629HT, The Netherlands
†§Von Kármán Institute for Fluid Dynamics, Rhode-St-Genèse, 1640, Belgium
‡¶Texas A&M University, College Station, TX 77843, USA

As the community investigates more complex flows with stronger streamwise variations and uses more physically inclusive stability techniques, such as BiGlobal theory, there is a perceived need for more accuracy in the base flows. To this end, the implication is that using these more advanced techniques, we are now including previously neglected terms of $O(1/\mathrm{Re}^2)$. Two corresponding questions follow: (1) how much accuracy can one reasonably achieve from a given set of basic-state equations and (2) how much accuracy does one need to converge more advanced stability techniques? The purpose of this paper is to generate base flow solutions to successively higher levels of accuracy and assess how inaccuracies ultimately affect the stability results. Basic states are obtained from solving the self-similar boundary-layer equations, and stability analyses with LST, which both share $O(1/\mathrm{Re})$ accuracy. This is the first step toward tackling the same problem for more complex basic states and more advanced stability theories. Detailed convergence analyses are performed, allowing to conclude on how numerical inaccuracies from the basic state ultimately propagate into the stability results for different numerical schemes and instability mechanisms at different Mach numbers.

Nomenclature

CF	Crossflow
CGL	Chebyshev-Gauss-Lobatto
DEKAF	Digits by Ethan, Koen, Alex, and Fernando
EPIC	Texas A&M's Euonymous Parabolized Instability Code
FD	Finite Difference
FD-q	q^{th}-order finite Difference
GICM	Groot-Illingworth-Chebyshev-Malik interpolation routine
LST	Linear Stability Theory
M1,M2	First and second Mack mode
PSE	Parabolized Stability Equations
QZ	Generalized Schur Decomposition
TS	Tollmein-Schlichting
VESTA	VKI Extensible Stability and Transition Analysis

Symbols

α	Streamwise perturbation wavenumbers
β	Spanwise perturbation wavenumbers
β_H	Hartree parameter
γ	Ratio of specific heats, c_p/c_v
δ^*	Displacement thickness
δ_e^*	Energy thickness
δ_h^*	Enthalpy thickness
ϵ	Measure of error
η	Self-similar wall-normal coordinate
θ	Non-dimensional streamwise semi-total enthalpy gradient
θ^*	Momentum thickness
κ	Thermal conductivity
λ	Second viscosity coefficient
μ	Dynamic viscosity

*Ph.D. student, Aerospace Engineering, TU Delft, k.j.groot@tudelft.nl, AIAA member
†Ph.D. student, Aeronautics and Aerospace, Von Kármán Institute for Fluid Dynamics, AIAA member
‡Ph.D. student, Aerospace Engineering, TAMU, AIAA member
§Research engineer, Aeronautics and Aerospace, Von Kármán Institute for Fluid Dynamics
¶Regents professor, Aerospace Engineering, TAMU, AIAA fellow

ξ	Marching streamwise coordinate
ρ	Mass density
ψ	Dimensional streamfunction
ω	Angular perturbation frequencies
$\mathcal{A}, \mathcal{B}, \mathcal{C}, \mathcal{D}, \mathcal{E}, \mathcal{F}$	Parameters for $\mathscr{F}(\eta)$
A	Jacobian matrix
a_0, a_1, a_2	Non-dimensional grouping parameters
C	Chapman-Rubesin parameter
$c.c.$	Complex conjugate
c_p	Specific heat at constant pressure
c_v	Specific heat at constant volume
D	Differentiation matrix
Ec	Eckert number, streamwise component
$\mathrm{Ec_w}$	Eckert number, spanwise component
$\mathscr{F}$	Initial guess for boundary layer profiles
f_η	Non-dimensional streamwise velocity component
g	Non-dimensional semi-total enthalpy
H	Semi-total enthalpy, $h + u^2/2$
h	Static enthalpy
H*	Shape factor
I	Integration matrix
j	Reciprocal of non-dimensional mass density
k	Non-dimensional spanwise velocity component
ℓ	Blasius length
M	Mach number of the freestream
N	Number of computational nodes in η domain
p	Static pressure
Pr	Prandtl number
$\overline{Q}$	Inviscid flow speed $\sqrt{\overline{u}_e^2 + \overline{w}_0^2}$
q	Instantaneous flow field state vector, or order of FD method
R	Right-hand-side vector
r	Recovery factor
Re	Reynolds number based on ℓ
$\mathrm{Re_x}$	Reynolds number based on x
S	Sutherland's constant
T	Temperature
t	Time coordinate
u	Streamwise velocity
v	Wall-normal velocity
w	Spanwise velocity
X	Computational space
x	Streamwise coordinate
y	Wall-normal coordinate
z	Spanwise coordinate
$\cdot'$	Perturbation flow variable
$\hat{\cdot}$	Newton-Raphson iterative perturbation variable
$\bar{\cdot}$	Base flow variable
$\tilde{\cdot}$	Newton-Raphson guessed-solution variable
$\tilde{\cdot}$	Perturbation flow variable
$\cdot_{,m}$	Index for given collocation node
$\cdot_0$	Constant reference value
$\cdot_\eta$	Differentiation with respect to η
$\cdot_{\max}$	Maximum value
$\cdot_{\mathrm{ref}}$	Reference value
$\cdot_{\overline{T}}$	Differentiation with respect to $\overline{T}$
$\cdot_\xi$	Differentiation with respect to ξ
$\cdot_{ad}$	Adiabatic value
$\cdot_{eig}$	Property of the eigensolver
$\cdot_e$	Boundary layer edge value
$\cdot_i$	Critical value or imaginary part
$\cdot_r$	Real part
$\cdot_w$	Wall value
$\cdot_y$	Differentiation with respect to y
$\lvert\cdot\rvert_\infty$	Infinity-norm
$\lvert\cdot\rvert_F$	Frobenius-norm

I. Introduction

BOUNDARY layer flow over solid surfaces undergoes laminar-turbulent transition at high enough Reynolds numbers, which is associated with a steep increase in skin friction and heat transfer. The latter are important design parameters, rendering transition prediction an important practice. The common approach to the prediction of transition on airfoils and nose cones is the combination of linear stability methods and the semi-empirical e^N-method, see Van Ingen[1] and Smith & Gamberoni.[2] Although finding its inception over 60 years ago, this technique is nowadays still the state-of-the-art for industrial applications.[3,4]

Stability methods can be split into several categories. The classical method, here referred to as the LST (Linear Stability Theory) approach, determines the stability characteristics captured in a velocity profile at a given streamwise location. Only the wall-normal gradient in the flow variables is accounted for, which is justified because the inherently neglected streamwise derivatives of slowly developing flows are small; the small parameter being 1/Re, where typically $\mathrm{Re} = \rho_e U_e \ell/\mu_e = \sqrt{\rho_e U_e x/\mu_e} = \sqrt{Re_x} = O(10^3)$. The PSE (Parabolized Stability Equation) method improves upon this by accounting for these so called non-parallel effects up to first order. This means that the model error associated to LST is $O(1/\mathrm{Re})$, while that of PSE is $O(1/\mathrm{Re}^2)$.

The BiGlobal approach accounts for all effects due to higher order streamwise derivatives of the flow and hence does not introduce a model error. In fact, the term with the smallest order of magnitude in the

BiGlobal system of equations for compressible flow is:[5]

$$\overline{T}\,\frac{\mathrm{Ec}}{\mathrm{Re}}\,\frac{\mathrm{d}\overline{\mu}}{\mathrm{d}\overline{T}}\left(\frac{\partial\overline{v}}{\partial x}\right)^2, \tag{1}$$

which, when $\partial/\partial x$ and $\overline{v}$ are $O(1/\mathrm{Re})$, is of $O(1/\mathrm{Re}^5)$. To be precise, the method yields a correction of $O(1/\mathrm{Re}^2)$ with respect to PSE, which means that numerical errors should be brought down to $o(1/\mathrm{Re}^2)$,[a] heuristically speaking, to isolate the otherwise neglected effects.

Substituting the BiGlobal approach for LST or PSE in their domain of applicability (i.e. slowly developing flows) is unnecessarily expensive, given the extra theoretical and numerical difficulties that have to be faced. This can only be justified when BiGlobal stability analysis is used for more complex, two-dimensional and streamwise inhomogeneous cases. However, the behavior of the spectrum provided and extra physical features accounted for by this method is incompletely understood, even for the simple flow cases like that over a flat plate.[6–10] Understanding the additional physical mechanisms accounted for in the BiGlobal method in simplified cases, however small, is essential before rigorous studies of more complex flows can be analyzed.

These methods require the prior computation of a base flow solution, and they are notorious for requiring a highly accurate solution of the basic state, see Reed *et al.*[11] Several arguments are given in the literature in this regard.

For BiGlobal analysis, the basic state needs to satisfy the Navier-Stokes equations, which is assumed in deriving the stability equations, see Theofilis.[12] The shear layers principally contributing to the production of perturbation energy need to be resolved, see Arnal,[13] and that the stability results must be converged as the resolution of the basic state is increased, see Reed *et al.*[11]

Basic questions remain, however, such as:

- Does grid convergence information of the base flow translate into convergence of the stability results?
- What is the effect of interpolating the base flow solution onto the stability grid?
- Do basic-state inaccuracies affect stability results computed with different numerical schemes equally?
- Do different instabilities and flow regimes require the same level of basic-state convergence and stability grid resolution?

The first endeavors in this direction must start at reconsidering self-similar boundary-layer solutions. Their accurate solution is highly important, because they will have to serve as either the initial condition to non-self-similar marching codes or boundary conditions for full Navier-Stokes solvers.[b]

The main goal of the current study is to investigate the required accuracy of these self-similar base flow profiles, corresponding to particular cases, to ensure a given intended accuracy for the stability results. To this end, the compressible variants of the self-similar Falkner-Skan-Cooke equations are solved by deploying the pseudo-spectral Chebyshev collocation method,[14–16] being a method prevalently deployed for the stability problem itself.[17,18] It provides maximal numerical (spectral order) accuracy per computational node. That way, performing this analysis is tractable over a large range of base flow accuracy. This allows estimating the error introduced by the base flow on the stability (classical LST) results. In turn, this enables generating benchmark results for a variety of instability mechanisms and flow regimes.

The paper is arranged as follows. First, the equations governing general self-similar compressible boundary-layer profiles and the associated instability modes are briefly revisited in section II. The numerical method is discussed in III, focusing on the preservation of the accuracy of the self-similar flow field on which the stability analysis is performed. The boundary-layer and stability results together with their associated error studies are presented in sections IV and V respectively.

II. Governing equations

A Cartesian coordinate system is presumed, respectively designating x, y and z as the streamwise, wall-normal and spanwise coordinates. The current interest supposes steady and spanwise invariant boundary-layer flow cases, implying the flow does not contain derivatives in z and time, t. The velocity components

[a] Here the small-o notation is implied: $o(\chi) \sim \epsilon < \chi$ and $O(\chi) \sim \epsilon \leqslant \chi$.

[b] Note that marching codes, solving the boundary-layer equations introduce a model error of $O(1/\mathrm{Re})$ as opposed to the model-error-free full Navier-Stokes problem.[6,7]

of these flows in the x-, y- and z-directions are denoted by $\overline{u}$, $\overline{v}$ and $\overline{w}$, respectively. The overbars are introduced for purposes of consistency with the stability framework. Evaluating variables at the edge of the boundary layer (attained for large wall-normal coordinates) is indicated with the subscript e. The edge-value corresponding to $\overline{w}$ is an exception to this, it is instead denoted by $\overline{w}_0$, because the aforementioned spanwise in-variance forces this value to be a global constant.

II.A. Self-similar boundary-layer equations

The compressible boundary-layer equations are stated as follows:

$$\overline{\rho}\,\overline{u}\frac{\partial\overline{u}}{\partial x}+\overline{\rho}\,\overline{v}\frac{\partial\overline{u}}{\partial y}=-\frac{\partial\overline{p}}{\partial x}+\frac{\partial}{\partial y}\left(\overline{\mu}\frac{\partial\overline{u}}{\partial y}\right), \tag{2a}$$

$$0=\frac{\partial\overline{p}}{\partial y}, \tag{2b}$$

$$\overline{\rho}\,\overline{u}\frac{\partial\overline{w}}{\partial x}+\overline{\rho}\,\overline{v}\frac{\partial\overline{w}}{\partial y}=\frac{\partial}{\partial y}\left(\overline{\mu}\frac{\partial\overline{w}}{\partial y}\right), \tag{2c}$$

$$\overline{\rho}\,\overline{u}\frac{\partial\overline{H}}{\partial x}+\overline{\rho}\,\overline{v}\frac{\partial\overline{H}}{\partial y}=\frac{\partial}{\partial y}\left(\overline{\mu}\,\overline{u}\,\frac{\partial\overline{u}}{\partial y}\right)+\overline{\mu}\left(\frac{\partial\overline{w}}{\partial y}\right)^2+\frac{\partial}{\partial y}\left(\overline{\kappa}\frac{\partial\overline{T}}{\partial y}\right), \tag{2d}$$

$$\frac{\partial\overline{\rho}\,\overline{u}}{\partial x}+\frac{\partial\overline{\rho}\,\overline{v}}{\partial y}=0. \tag{2e}$$

Here $\overline{H}$ denotes the semi-total enthalpy.[c] Far enough from the leading edge, boundary layers develop slowly in the streamwise direction, allowing the solution profiles to settle into a shape independent of x. The equations governing these self-similar profiles are obtained by using the Illingworth transformation.[d]

This expresses the equations in function of the self-similar η and marching ξ variables, which relate to x and y through:

$$\mathrm{d}\eta(x,y)=\frac{\overline{u}_e(x)}{\sqrt{2\xi(x)}}\overline{\rho}(x,y)\mathrm{d}y;\qquad \mathrm{d}\xi(x)=\overline{\rho}_e(x)\,\overline{u}_e(x)\,\overline{\mu}_e(x)\,\mathrm{d}x. \tag{3}$$

Partial derivatives with respect to ξ and η will hereafter be denoted with the subscripts ξ and η, respectively.

Furthermore, the following non-dimensional variables are introduced for the streamwise and spanwise velocity components and the (semi-total) enthalpy:

$$f_\eta(\xi,\eta)=\overline{u}/\overline{u}_e;\qquad k(\xi,\eta)=\overline{w}/\overline{w}_0;\qquad g(\xi,\eta)=\overline{H}/\overline{H}_e. \tag{4}$$

The variable f is originally related to the dimensional stream-function: $\overline{\psi}=f\sqrt{2\xi}$, whose existence implies inherently satisfying the continuity equation.

By expressing the boundary-layer equations in the self-similarity coordinates, one obtains the compressible equivalents of the Falkner-Skan-Cooke equations:

$$(C\,f_{\eta\eta})_\eta+f f_{\eta\eta}+\beta_H(j-f_\eta^2)=2\xi\,(f_\eta f_{\xi\eta}-f_{\eta\eta}f_\xi) \tag{5a}$$

$$(C\,k_\eta)_\eta+f k_\eta=2\xi\;\;(f_\eta k_\xi-k_\eta f_\xi) \tag{5b}$$

$$(a_1\,g_\eta)_\eta+f g_\eta-\theta f_\eta g-(a_2 f_\eta f_{\eta\eta})_\eta+a_0k_\eta^2=2\xi\;\;(f_\eta g_\xi-g_\eta f_\xi) \tag{5c}$$

Here: $j=\overline{\rho}_e/\overline{\rho}=j(g)$, the Hartree parameter β_H represents the streamwise pressure gradient, the Chapman-Rubesin parameter C denotes the density-viscosity profile, θ represents the streamwise semi-total enthalpy gradient, and a_0, a_1 and a_2 are grouping parameters. All are respectively defined as follows:

$$\beta_H=\frac{2\xi}{\overline{u}_e}\frac{\mathrm{d}\overline{u}_e}{\mathrm{d}\xi},\qquad C=\frac{\overline{\rho}\,\overline{\mu}}{\overline{\rho}_e\overline{\mu}_e},\qquad \theta=\frac{2\xi}{\overline{H}_e}\frac{\mathrm{d}\overline{H}_e}{\mathrm{d}\xi},$$
$$a_0=\frac{\mathrm{Ec}_w}{1+\mathrm{Ec}/2}\,C,\qquad a_1=\frac{C}{\mathrm{Pr}},\qquad a_2=\mathrm{Ec}\frac{1-1/\mathrm{Pr}}{1+\mathrm{Ec}/2}\,C. \tag{6}$$

[c]The semi-total enthalpy $\overline{H}=\overline{h}+\overline{u}^2/2$ considers only the streamwise component of the kinematic energy, not the spanwise component $(\overline{w}^2/2)$.

[d]The name of this transformation is referred to differently in different references. We consider what is referred to as the Levy-Lees transformation by Schlichting *et al.* [19, p. 247], the Lees-Dorodnitsyn transformation by Anderson [20, p. 279] and the Illingworth transformation by White [21, p. 511].

Furthermore, $\mathrm{Ec} = \overline{u}_e^2/\overline{h}_e$ and $\mathrm{Ec}_w = \overline{w}_0^2/\overline{h}_e$ denotes the streamwise and spanwise Eckert number, M is the freestream Mach number and $\mathrm{Pr} = c_p\overline{\mu}_e/\overline{\kappa}_e$ represents the Prandtl number. The total enthalpy in the freestream is presumed to be conserved, which imposes $\theta = 0$. This is equivalent to enforcing Euler's energy conservation equation in the freestream.[e,f]

Throughout this paper, the flow is assumed to be calorically perfect. The boundary-layer assumptions require the pressure to be constant in the wall-normal direction (Eq. 2b). The equation of state therefore imposes that the density must be inversely proportional to the temperature. Furthermore, Sutherland's law is used as the closure relationship for the dynamic viscosity, $\overline{\mu}$, Stokes's hypothesis is used for the second viscosity coefficient, $\overline{\lambda}$,[g] and the thermal conductivity, $\overline{\kappa}$, follows by assuming a constant Prandtl number. This can be expressed as:

$$\frac{\overline{\rho}}{\overline{\rho}_e} = \frac{\overline{T}_e}{\overline{T}}, \quad \frac{\overline{\mu}(\overline{T})}{\overline{\mu}_{\mathrm{ref}}} = \left(\frac{\overline{T}}{\overline{T}_{\mathrm{ref}}}\right)^{\frac{3}{2}} \frac{\overline{T}_{\mathrm{ref}} + S}{\overline{T} + S}, \qquad \frac{\overline{\lambda}}{\overline{\lambda}_e} = -\frac{2}{3}\frac{\overline{\mu}}{\overline{\mu}_e} \qquad \frac{\overline{\kappa}}{\overline{\kappa}_e} = \frac{\overline{\mu}}{\overline{\mu}_e}. \tag{7}$$

where $\overline{\mu}_{\mathrm{ref}}$ and $\overline{T}_{\mathrm{ref}}$ are a reference viscosity and temperature, respectively, and S is the Sutherland constant. Note that $\overline{\mu}_e = \overline{\mu}(\overline{T}_e) \neq \overline{\mu}_{\mathrm{ref}}$.

The ξ-derivatives, forming the right hand side terms of system (5), encode the solutions' streamwise history. Self-similar solutions are sought in this study, which requires dropping these terms.

The system is completed with the following edge and wall boundary conditions:

$$\lim_{\eta\to\infty} f_\eta(\eta) = 1, \qquad f(0) = f_\eta(0) = 0, \qquad \lim_{\eta\to\infty} k(\eta) = 1, \qquad k(0) = 0, \qquad \lim_{\eta\to\infty} g(\eta) = 1, \tag{8}$$

whereas the following conditions respectively portray an iso-thermal or adiabatic wall condition:

$$g(0) = g_w, \quad \text{or} \quad g_\eta(0) = 0, \tag{9}$$

where g_w represents the non-dimensional semi-total enthalpy at the wall.

II.B. Stability problem

The boundary-layer solution constitutes the laminar base flow for this problem. If a low disturbance environment is present, one can decompose the instantaneous flow field, denoted as q, into the laminar base flow, $\overline{q}$, and a linear perturbation field, q':

$$q = \overline{q} + q', \tag{10}$$

and $q' \ll \overline{q}$. That is, the perturbation is assumed to be infinitesimally small with respect to the base flow, which naturally leads to (linear) stability methods.

As elaborated upon before, the variations in the base flow in the x-direction, time and the spanwise z-direction are discarded. This assumption allows using the classical Fourier ansatz associated to the LST analysis:

$$q' = \tilde{q}(y)\, e^{i(\alpha x + \beta z - \omega t)} + c.c., \tag{11}$$

Here $\tilde{q} = [\tilde{u}\ \tilde{v}\ \tilde{w}\ \tilde{T}\ \tilde{p}]^T$ are the perturbation amplitude y-profiles, α and β are the streamwise and spanwise wavenumbers and ω is the angular frequency of the perturbation. *c.c.* abbreviates the operation of taking the complex conjugate. The wavenumber β should not be confused with the Hartree parameter, β_H. In general, α and ω are considered to be complex, where $-\alpha_i$ and ω_i respectively represent the exponential perturbation amplification in the x-direction and time. The amplitude function $\tilde{q}$ is merely the shape of the wave in y and is normalized to have maximal magnitude 1. The spatial stability problem is considered here,

[e] Note that since $\mathrm{d}\overline{w}_0/\mathrm{d}\xi = 0$, the semi-total enthalpy gradient $\mathrm{d}\overline{H}_e/\mathrm{d}\xi$ is identical to the total enthalpy gradient.

[f] If this is not enforced, as $\eta \to \infty$, g approaches the asymptotic value at an algebraic as opposed to exponential rate, which is illustrated as follows. Consider a calorically perfect freestream, i.e. $j = g$ and $f_\xi, f_{\eta\eta}, k_\eta, g_\xi, g_\eta$ and higher order η-derivatives all approach 0. That is, these variables are negligibly small. The term fg_η, however, remains finite due to $f \sim \eta$. In this case, equation (5c) simplifies to $g_\eta/g = \theta f_\eta/f$, which can be solved to yield: $g = c^{\mathrm{st}} f^\theta$, where $c^{\mathrm{st}} = \lim_{\eta\to\infty} 1/f(\eta)^\theta$, so to satisfy the condition $\lim_{\eta\to\infty} g(\eta) = 1$. If $\theta = 0$, this behavior is nullified.

[g] Note that this variable does not appear in system (5), but it does in the stability problem.

which implies that one solves for $\alpha \in \mathbb{C}$, while $\omega, \beta \in \mathbb{R}$ are given. The perturbation solutions are governed by the compressible LST equations:

$$\begin{aligned}
&\frac{i\,\beta\,\gamma\,\tilde{u}\,\mathrm{M}^2\,\overline{p}\,\overline{w}}{\overline{T}} + \frac{\gamma\,\tilde{v}\,\mathrm{M}^2\,\overline{p}\,\overline{u}_y}{\overline{T}} + \frac{i\,\alpha\,\gamma\,\tilde{u}\,\mathrm{M}^2\,\overline{p}\,\overline{u}}{\overline{T}} - \frac{i\,\gamma\,\omega\,\tilde{u}\,\mathrm{M}^2\,\overline{p}}{\overline{T}} = \frac{\tilde{T}\,\overline{\mu}_{\overline{T}}\,\overline{u}_{y\,y}}{\mathrm{Re}} \\
&+\frac{\tilde{T}\,\overline{\mu}_{\overline{T}\,\overline{T}}\,\overline{T}_y\,\overline{u}_y}{\mathrm{Re}} + \frac{\tilde{T}_y\,\overline{\mu}_{\overline{T}}\,\overline{u}_y}{\mathrm{Re}} + \frac{i\,\alpha\,\tilde{v}\,\overline{\mu}_{\overline{T}}\,\overline{T}_y}{\mathrm{Re}} + \frac{\tilde{u}_y\,\overline{\mu}_{\overline{T}}\,\overline{T}_y}{\mathrm{Re}} - i\,\alpha\,\tilde{p} - \frac{\alpha\,\beta\,\tilde{w}\,\overline{\mu}}{\mathrm{Re}} + \frac{i\,\alpha\,\tilde{v}_y\,\overline{\mu}}{\mathrm{Re}} \\
&+\frac{\tilde{u}_{y\,y}\,\overline{\mu}}{\mathrm{Re}} - \frac{\beta^2\,\tilde{u}\,\overline{\mu}}{\mathrm{Re}} - \frac{2\,\alpha^2\,\tilde{u}\,\overline{\mu}}{\mathrm{Re}} - \frac{\alpha\,\beta\,\tilde{w}\,\overline{\lambda}}{\mathrm{Re}} + \frac{i\,\alpha\,\tilde{v}_y\,\overline{\lambda}}{\mathrm{Re}} - \frac{\alpha^2\,\tilde{u}\,\overline{\lambda}}{\mathrm{Re}},
\end{aligned} \tag{12a}$$

$$\begin{aligned}
&\frac{i\,\beta\,\gamma\,\tilde{v}\,\mathrm{M}^2\,\overline{p}\,\overline{w}}{\overline{T}} + \frac{i\,\alpha\,\gamma\,\tilde{v}\,\mathrm{M}^2\,\overline{p}\,\overline{u}}{\overline{T}} - \frac{i\,\gamma\,\omega\,\tilde{v}\,\mathrm{M}^2\,\overline{p}}{\overline{T}} = \frac{i\,\beta\,\tilde{T}\,\overline{\mu}_{\overline{T}}\,\overline{w}_y}{\mathrm{Re}} + \frac{i\,\alpha\,\tilde{T}\,\overline{\mu}_{\overline{T}}\,\overline{u}_y}{\mathrm{Re}} \\
&+\frac{2\,\tilde{v}_y\,\overline{\mu}_{\overline{T}}\,\overline{T}_y}{\mathrm{Re}} + \frac{i\,\beta\,\tilde{w}\,\overline{\lambda}_{\overline{T}}\,\overline{T}_y}{\mathrm{Re}} + \frac{\tilde{v}_y\,\overline{\lambda}_{\overline{T}}\,\overline{T}_y}{\mathrm{Re}} + \frac{i\,\alpha\,\tilde{u}\,\overline{\lambda}_{\overline{T}}\,\overline{T}_y}{\mathrm{Re}} - \tilde{p}_y + \frac{i\,\beta\,\tilde{w}_y\,\overline{\mu}}{\mathrm{Re}} + \frac{2\,\tilde{v}_{y\,y}\,\overline{\mu}}{\mathrm{Re}} \\
&-\frac{\beta^2\,\tilde{v}\,\overline{\mu}}{\mathrm{Re}} - \frac{\alpha^2\,\tilde{v}\,\overline{\mu}}{\mathrm{Re}} + \frac{i\,\alpha\,\tilde{u}_y\,\overline{\mu}}{\mathrm{Re}} + \frac{i\,\beta\,\tilde{w}_y\,\overline{\lambda}}{\mathrm{Re}} + \frac{\tilde{v}_{y\,y}\,\overline{\lambda}}{\mathrm{Re}} + \frac{i\,\alpha\,\tilde{u}_y\,\overline{\lambda}}{\mathrm{Re}},
\end{aligned} \tag{12b}$$

$$\begin{aligned}
&\frac{\gamma\,\tilde{v}\,\mathrm{M}^2\,\overline{p}\,\overline{w}_y}{\overline{T}} + \frac{i\,\beta\,\gamma\,\tilde{w}\,\mathrm{M}^2\,\overline{p}\,\overline{w}}{\overline{T}} + \frac{i\,\alpha\,\gamma\,\tilde{w}\,\mathrm{M}^2\,\overline{p}\,\overline{u}}{\overline{T}} - \frac{i\,\gamma\,\omega\,\tilde{w}\,\mathrm{M}^2\,\overline{p}}{\overline{T}} = \frac{\tilde{T}\,\overline{\mu}_{\overline{T}}\,\overline{w}_{y\,y}}{\mathrm{Re}} \\
&+\frac{\tilde{T}\,\overline{\mu}_{\overline{T}\,\overline{T}}\,\overline{T}_y\,\overline{w}_y}{\mathrm{Re}} + \frac{\tilde{T}_y\,\overline{\mu}_{\overline{T}}\,\overline{w}_y}{\mathrm{Re}} + \frac{\tilde{w}_y\,\overline{\mu}_{\overline{T}}\,\overline{T}_y}{\mathrm{Re}} + \frac{i\,\beta\,\tilde{v}\,\overline{\mu}_{\overline{T}}\,\overline{T}_y}{\mathrm{Re}} - i\,\beta\,\tilde{p} + \frac{\tilde{w}_{y\,y}\,\overline{\mu}}{\mathrm{Re}} - \frac{2\,\beta^2\,\tilde{w}\,\overline{\mu}}{\mathrm{Re}} \\
&-\frac{\alpha^2\,\tilde{w}\,\overline{\mu}}{\mathrm{Re}} + \frac{i\,\beta\,\tilde{v}_y\,\overline{\mu}}{\mathrm{Re}} - \frac{\alpha\,\beta\,\tilde{u}\,\overline{\mu}}{\mathrm{Re}} - \frac{\beta^2\,\tilde{w}\,\overline{\lambda}}{\mathrm{Re}} + \frac{i\,\beta\,\tilde{v}_y\,\overline{\lambda}}{\mathrm{Re}} - \frac{\alpha\,\beta\,\tilde{u}\,\overline{\lambda}}{\mathrm{Re}},
\end{aligned} \tag{12c}$$

$$\begin{aligned}
&\frac{i\,\beta\,\gamma\,\tilde{T}\,\mathrm{M}^2\,\overline{p}\,\overline{w}}{\overline{T}} + \frac{i\,\alpha\,\gamma\,\tilde{T}\,\mathrm{M}^2\,\overline{p}\,\overline{u}}{\overline{T}} + \frac{\gamma\,\tilde{v}\,\mathrm{M}^2\,\overline{p}\,\overline{T}_y}{\overline{T}} - \frac{i\,\gamma\,\omega\,\tilde{T}\,\mathrm{M}^2\,\overline{p}}{\overline{T}} \\
&= \frac{(\gamma-1)\,\tilde{T}\,\mathrm{M}^2\,\overline{\mu}_{\overline{T}}\,(\overline{w}_y)^2}{\mathrm{Re}} + \frac{2\,(\gamma-1)\,\tilde{w}_y\,\mathrm{M}^2\,\overline{\mu}\,\overline{w}_y}{\mathrm{Re}} + \frac{2\,i\,\beta\,(\gamma-1)\,\tilde{v}\,\mathrm{M}^2\,\overline{\mu}\,\overline{w}_y}{\mathrm{Re}} \\
&+i\,\beta\,(\gamma-1)\,\mathrm{M}^2\,\tilde{p}\,\overline{w} + \frac{(\gamma-1)\,\tilde{T}\,\mathrm{M}^2\,\overline{\mu}_{\overline{T}}\,(\overline{u}_y)^2}{\mathrm{Re}} + \frac{2\,i\,\alpha\,(\gamma-1)\,\tilde{v}\,\mathrm{M}^2\,\overline{\mu}\,\overline{u}_y}{\mathrm{Re}} \\
&+\frac{2\,(\gamma-1)\,\tilde{u}_y\,\mathrm{M}^2\,\overline{\mu}\,\overline{u}_y}{\mathrm{Re}} + i\,\alpha\,(\gamma-1)\,\mathrm{M}^2\,\tilde{p}\,\overline{u} + \frac{\tilde{T}\,\overline{\kappa}_{\overline{T}}\,\overline{T}_{y\,y}}{\mathrm{Pr}\,\mathrm{Re}} + \frac{\tilde{T}\,\overline{\kappa}_{\overline{T}\,\overline{T}}\,(\overline{T}_y)^2}{\mathrm{Pr}\,\mathrm{Re}} \\
&+\frac{2\,\tilde{T}_y\,\overline{\kappa}_{\overline{T}}\,\overline{T}_y}{\mathrm{Pr}\,\mathrm{Re}} + \frac{\tilde{T}_{y\,y}\,\overline{\kappa}}{\mathrm{Pr}\,\mathrm{Re}} - \frac{\beta^2\,\tilde{T}\,\overline{\kappa}}{\mathrm{Pr}\,\mathrm{Re}} - \frac{\alpha^2\,\tilde{T}\,\overline{\kappa}}{\mathrm{Pr}\,\mathrm{Re}} \\
&-i\,(\gamma-1)\,\omega\,\mathrm{M}^2\,\tilde{p} + (\gamma-1)\,\tilde{v}\,\mathrm{M}^2\,\overline{p}_y,
\end{aligned} \tag{12d}$$

$$\begin{aligned}
&-\frac{i\,\beta\,\tilde{T}\,\overline{w}}{\overline{T}} + \frac{i\,\beta\,\tilde{p}\,\overline{w}}{\overline{p}} - \frac{i\,\alpha\,\tilde{T}\,\overline{u}}{\overline{T}} + \frac{i\,\alpha\,\tilde{p}\,\overline{u}}{\overline{p}} - \frac{\tilde{v}\,\overline{T}_y}{\overline{T}} \\
&+\frac{i\,\omega\,\tilde{T}}{\overline{T}} - \frac{i\,\omega\,\tilde{p}}{\overline{p}} + \frac{\tilde{v}\,\overline{p}_y}{\overline{p}} + i\,\beta\,\tilde{w} + \tilde{v}_y + i\,\alpha\,\tilde{u} = 0.
\end{aligned} \tag{12e}$$

These equations are obtained by linearizing the Navier-Stokes equations about the boundary-layer base flow and incorporating the Fourier ansatz (11). Note that the linearized continuity equation has been simplified by dividing all terms by $\overline{\rho} = \gamma\,M^2\,\overline{p}/\overline{T}$. This improved the norm of the corresponding matrix system, which resulted in a decrease of the Frobenius norm, and therefore a minimum eigenvalue error, of several orders of magnitude.

As for the wall boundary conditions applied to the amplitude variables, no-slip boundary conditions are specified for the velocity amplitudes, $\tilde{u}(0)$, $\tilde{v}(0)$, and $\tilde{w}(0)$, and a compatibility condition[h] is used for the pressure amplitude $\tilde{p}(0)$. For the cases where $\omega_r \neq 0$, it is physically justified to specify a homogeneous Dirichlet condition on the wall temperature, $\tilde{T}(0)$, independently from the basic-state thermal wall condition.[i]

The treatment of the free-stream boundaries also varies among the different research groups. Typical approaches are to consider Dirichlet conditions on all perturbation amplitudes except for the pressure amplitude (accounted for through a compatibility condition),[18,23] or Neumann conditions on all amplitudes.[22,24,35]

III. Numerical methodology

Having elaborated upon the governing equations, this section describes the numerical methodology deployed in solving them. First finite-difference and Chebyshev discretizations, together with the Runge-Kutta methods are discussed. Second, the DEKAF boundary-layer solver is introduced. A consistent interpolation technique is then presented, and finally the set-up and Newton-Raphson solution method are treated. The latter requires the prescription of an initial guess of the solution, which is elaborated upon last.

[h] Typical examples of used compatibility conditions are the linearized continuity or wall-normal momentum equation, evaluated at the wall.[22]

[i] For the high perturbation frequencies usually considered, the thermal inertia of the wall resists any heat absorption.[22] For the stationary crossflow instability, the frequency is equal to zero, so this reasoning does not apply. However, in the current paper this instability is considered in incompressible flow conditions only. In this situation, the effect of the temperature perturbation is negligible, again justifying the use of a homogeneous Dirichlet condition on $\tilde{T}(0)$.

III.A. Discretization methods

Finite-difference methods are foundational to many numerical algorithms for solving differential equations. The central idea is to substitute derivatives (e.g., $\partial f/\partial x$) by ratios of finite differences ($\Delta f/\Delta x$).[25] These differences may be expressed on a given computational stencil corresponding to a certain order of accuracy, provided the discretization is mathematically convergent to the original differential equation. Over an interval, state variables of a differential equation may be discretized, which can then be formulated as a matrix equation that can be solved with standard linear algebra techniques.[26]

Chebyshev collocation equips Chebyshev-Gauss-Lobatto (CGL) nodes,[14] which provide *"an optimal placing of interpolating points to minimize the error in Lagrange interpolation"*, see Burden & Faires.[27] Since it uses the complete node stencil to determine the derivative at a collocation node, it yields spectrally accurate approximations. For more details on the discretization method, see Trefethen,[15] Canuto *et al.*[14] and Orszag.[17]

Often in computational science, Runge-Kutta methods are used to numerically integrate differential equations.[28] These algorithms can be characterized by combining several finite-difference steps, each involving an evaluation of the differential equation, and then matching a higher-order Taylor series.[26] However, these methods can require significant amounts of computer time, even if the solution propagation is monitored for adaptively changing the finite-difference step-sizes. Despite this they remain a common numerical technique for laminar basic-state resolution.[29]

III.B. DEKAF boundary-layer solver

The boundary-layer equations (5) with the self-similarity simplifications are solved using the DEKAF (Digits by Ethan, Koen, Alex and Fernando) boundary-layer solver. It uses a Chebyshev pseudo-spectral discretization on the linearized boundary-layer equations, which are solved with a Newton-Raphson method (see § III.D). Function suites provided by Weidemann & Reddy[16] are used to compute the differentiation matrices and perform Lagrangian interpolation with Chebyshev polynomials.

To provide a higher resolution of the boundary layer, the mapping introduced by Malik[18] is used in the η-space. That is, both the CGL node distribution and the differentiation matrices, as originally defined on the computational X-space spanning $[-1, 1]$, are transformed to the domain $[0, \eta_{\max}]$ in η-space. The interior coordinate η_i is defined, which splits the domain in two parts, each containing half the number of nodes. It is a common practice to place this coordinate at the edge of the boundary layer. One can then retrieve dimensional quantities by undoing the Illingworth transformation (3). The necessary integration for the inverse Illingworth transformation is done while retaining spectral accuracy by inverting the Chebyshev differentiation matrix (see Appendix A).

III.C. GICM interpolation

Equation (3) illustrates that the density has an impact on the scaling of y with respect to η. Usually $\overline{\rho} < \overline{\rho}_e$ inside the boundary layer, meaning that the distance between nodes in the η-grid will be stretched as they are mapped to the y-grid. This poses an important implication for the location of the collocation nodes. If η-nodes are generated and mapped to the y-space, they do not align with y-nodes, that are originally generated in the y-space, even though the same y_i and $y_{\max}$ are used. This in-equivalence can be illustrated as follows. Let m be the index corresponding to a particular collocation node:

$$
\begin{array}{lllll}
X_{CGL,m} \in [-1\ 0\ 1] & \overset{\text{Malik}}{\mapsto} \eta_{1,m} \in [0\ \eta_i\ \eta_{\max}] & \overset{\text{Illingworth}}{\mapsto} & y_{1,m} & \in [0\ y_i\ y_{\max}] \\
 & & & \nparallel & \\
X_{CGL,m} \in [-1\ 0\ 1] & \overset{\text{Malik}}{\mapsto} & & y_{2,m} & \in [0\ y_i\ y_{\max}].
\end{array}
$$

For all $y_{2,m} \neq 0$, y_i or $y_{\max}$, $y_{2,m}$ is unequal to $y_{1,m}$ in general. For this reason, having to interpolate the solution is inevitable.

This is where the optimal Lagrangian interpolation properties of the Chebyshev CGL-nodes are highly beneficial. The interpolation is naturally performed by passing from the node X_{CGL}-coordinates (corresponding to y_1) to the X_2-coordinates (corresponding to y_2). To obtain the latter X_2-coordinates, one must perform the inverses of the Illingworth transformation and Malik mapping (noted Illingworth^{-1} and Malik^{-1},

respectively):

$$X_{2,m} \overset{\text{Malik}^{-1}}{\longleftarrow} \eta_{2,m} \overset{\text{Illingworth}^{-1}}{\longleftarrow} y_{2,m}. \tag{13}$$

The inverse Illingworth transformation depends on the density $\overline{\rho}$ evaluated on the y_2-nodes, however. So, an iterative procedure is set up that updates the latter $\overline{\rho}$-values. A spline interpolation from the y_1- to the y_2-nodes is performed as the initial guess, while the Lagrangian interpolation is used in subsequent steps. The procedure is repeated up to the point where machine precision convergence is attained for the X_2-node positions. These nodes are thereafter used to perform the final interpolation to the y_2-node positions. This interpolation method is from now on referred to as the Groot-Illingworth-Chebyshev-Malik (GICM) interpolation routine. Its performance is assessed among the results.

Note that this interpolation is applicable to any y_2 grid, as long as it is accompanied by an appropriate and integrable differentiation matrix via the method described in Appendix A. One of its main advantages is that it retains the spectral accuracy of the solution, through the use of the Lagrangian interpolation methodology, independently from the size of the objective y_2 grid. Boundary-layer solution profiles are generally rather simple, and require a lower number of points than instability mode shapes. The GICM interpolation accordingly allows for an optimal usage of grid points in both the basic-state and stability problem, with negligible accuracy loss when transferring between grids. Moreover, it is also flexible with respect to whichever numerical scheme is used to solve the stability problem (see § III.A).

III.D. Equation set-up and solution method

The numerical set-up applied here is a Newton-Raphson approach, based on directly inverting the linearized Falkner-Skan-Cooke problem; i.e. the related Jacobian matrix. Just like the stability approach, a small perturbation is applied to the variables, f, k and g, e.g.:

$$f(\eta) = \overline{\overline{f}}(\eta) + \check{f}(\eta), \tag{14}$$

where $\overline{\overline{f}}$ is referred to as a pseudo-basic-state quantity and $\check{f}$ is the (*steady*, spatial) fluctuation. An initial guess is made for the pseudo-basic-state quantities, which are detailed in § III.E.

After substituting this expansion into system (5) and dropping the non-linear terms in the fluctuations, a linear system of equations is obtained, that can be written as:

$$\overline{\overline{A}}\check{F} = -\overline{\overline{R}}, \tag{15}$$

where $\check{F} = [\check{f}_\eta, \check{f}, \check{k}, \check{g}]^T$. That is, $\check{f}_\eta$ and $\check{f}$ are treated as separate variables. This choice for $\check{F}$ results in a matrix with at most second order differentiation matrices. This improved the conditioning of the resulting problem significantly over using third order differentiation matrices, resulting in lower residuals when performing Newton-Raphson iterations.

The Jacobian matrix $\overline{\overline{A}}$ and the right hand side vector $\overline{\overline{R}}$ only contain variables with double overbars, these overbars are dropped in the remainder of this section for notation convenience. In particular, A contains the coefficients multiplying the linear fluctuation quantities. The non-zero entries of the right hand side or residual term, R, consist of a copy of system (5) evaluated on the pseudo-basic-state quantities. Next to the equation residuals, R contains zeros in the rows corresponding to f_η, which describe the evaluation of the derivative $\check{f}_\eta = D\check{f}$.

As a first step, the matrix A is built such that system (5) is evaluated on all collocation points, including the boundaries. Due to the explicit appearance of the derivatives of the solution variables in the spectral collocation method, as a second step, the boundary conditions (8) and (9) are applied by replacing the differential equation evaluated at the boundary of interest by the boundary condition. In the initial guess of the pseudo-basic-state variables, special care is invested in ensuring that the initial guesses/conditions satisfy the boundary conditions identically. Hence, the boundary conditions for the fluctuation quantities are homogeneous and the corresponding rows in R contain zeros.

If the pseudo-basic-state quantities satisfy system (5), R evaluates to zero and the invertibility of A then implies that $\check{F} = 0$. If $R \neq 0$, a Newton-Raphson iteration yields the fluctuation vector $\check{F} = A^{-1}R$, which represents the required distortion of the pseudo-basic-state variables to bring R closer to zero. These Newton-Raphson iterations are continued up to the point where all variables, including the involved derivatives and transport coefficients, are converged to machine precision.

The link between the linear stability approach and the set-up of the Newton-Raphson method deserves mentioning. Note that equation (14) is recovered when substituting $\alpha = \omega = \beta = 0$ into equation (11). The complex exponential evaluates to unity, so the implied complexification is annihilated. In essence, the Newton-Raphson scheme corresponds to a reduced stability problem for infinitely long structures in the streamwise, spanwise and temporal directions; the self-similar, spanwise invariant and steady base flow problem.

III.E. Initial conditions

To form the first instance of R in system (14), an initial guess for the pseudo-basic-state quantities is required. The convergence of the method was observed to be highly dependent on the quality of this initial guess. The smaller the difference between the initial guess and the final solution, the higher the convergence rate to the desired solutions. If the initial difference is too large, convergence to other, spuriously oscillatory, solutions may result.

In order to avoid these spurious solutions, first, the unequivocal satisfaction of the boundary conditions is paramount. Second, an initial guess based on the shape of boundary-layer profiles is used. A canonical polynomial-exponential function is used for the initial guess for f_η, g and k:

$$\mathscr{F}(\eta) = 1 + (\mathcal{A}\eta^3 + \mathcal{B}\eta^2 + \mathcal{C}\eta + \mathcal{D})\mathrm{e}^{-\mathcal{E}\eta^2+\mathcal{F}\eta}\,. \tag{16}$$

where $\mathcal{A}$, $\mathcal{B}$, $\mathcal{C}$, $\mathcal{D}$, $\mathcal{E}$ and $\mathcal{F}$ are parameters, where $\mathcal{E} \neq 0$ in all cases. Hence, the function $\mathscr{F}(\eta)$ approaches unity (super-)exponentially as $\eta \to \infty$; automatically satisfying the freestream behavior and boundary condition.

The parameters $\mathcal{B}$, $\mathcal{D}$, and $\mathcal{F}$ are fixed by the wall boundary condition on the function value and derivatives, while the complementary parameters $\mathcal{A}$, $\mathcal{C}$, and $\mathcal{E}$ are obtained by fitting $\mathscr{F}(\eta)$ to several boundary-layer solutions for a larger range of different Mach numbers and wall temperature ratios. To this end, VESTA's fourth-order Runge-Kutta boundary-layer solver[23] was used to obtain f_η, and g profiles, keeping $\beta_H = \overline{w}_0 = 0$. The initial condition for k is taken identical to that for f_η.

A sample of the parameters $\mathcal{A}$, $\mathcal{C}$, and $\mathcal{E}$ is presented in tables 1 and 2. For test conditions other than the computed ones, the set of parameters corresponding to the closest *lower* Mach number is taken. For instance, to run M = 5.8, the parameter set corresponding to M = 5 is used. This demonstrated to yield better convergence rates than when interpolating the reported values.[j] For the subsonic cases detailed in table 4, the initial condition for g was taken to be a simple 1^{st}-order polynomial satisfying its two boundary conditions.

III.F. Stability codes

Three independent stability codes were used in executing the current study. In particular, VESTA (the VKI Extensible Stability and Transition Analysis toolkit), the in-house stability code of TU Delft and EPIC (the Euonymous Parabolized Instability Code).

The underlying principles of the stability solver in VESTA and the in-house stability solver of TU Delft are very similar. Their description is reported elsewhere.[23,30] VESTA and the TU Delft code are scheme-independent, meaning that any discretization method can be used. For the majority of cases, Chebyshev spectral collocation is used in these codes to solve the stability problem. In fact, the set-up of the self-similar basic-state problem is directly analogous to the implementations of these codes; they provided the inspiration for creating the DEKAF solver. The stability problem is solved using the QZ algorithm.[31,32]

EPIC is a compressible nonlinear parabolized stability equations (NPSE) solver in general three-dimensional curvilinear coordinates that features additional linearized parabolized stability equations (LPSE) and linear stability theory capability. EPIC has been used to analyze the stability of various boundary-layer instabilities (e.g., first and second Mack modes and the crossflow instability) over three-dimensional geometries, such as elliptic cones or yawed straight circular cones. Further details are given in the thesis of Oliviero[24] and the dissertation of Kocian.[33] For the analysis performed in this paper, EPIC uses fourth-order finite-difference schemes to evaluate derivative of basic-state and stability quantities throughout the boundary-layer interior nodes, whereas second order schemes are used at the wall and freestream nodes, and their wall-normal neighbors. The stability problem is solved using the Arnoldi iteration algorithm, which is accurate to $O(10^{-13})$.[34]

[j] Experience shows that using g profiles attaining values lower than the final profile is beneficial for the convergence behavior.

Table 1. Sample of coefficients for the initial guess function $\mathscr{F}(\eta)$ (Eq. 16) for f_η for adiabatic wall conditions and for several edge Mach numbers. Values of $f_{\eta\eta,w}$, used to obtain $\mathcal{B}$, $\mathcal{D}$, and $\mathcal{F}$ are also listed. $f_{\eta\eta\eta,w}$ and f_w values are omitted since $f_{\eta\eta\eta,w} = f_w = 0$ for a non-blowing adiabatic wall with $\beta_H = 0$.

M_e	$\mathcal{A}$	$\mathcal{C}$	$\mathcal{E}$	$f_{\eta\eta,w}$
0.01	4.07811e-02	9.44090e-02	5.19947e-01	4.69601e-01
0.5	4.05977e-02	9.00186e-02	5.20458e-01	4.72501e-01
1	4.00238e-02	7.62938e-02	5.21708e-01	4.81145e-01
2	3.86102e-03	-1.35885e-01	5.71351e-01	5.13780e-01
3	2.37842e-03	-2.61074e-01	5.59809e-01	5.60286e-01
4	-1.02949e-01	-8.57249e-01	5.06635e-01	6.12808e-01
5	-3.53516e-01	-1.42533e+00	4.20244e-01	6.66609e-01
6	-7.14969e-01	-1.84294e+00	3.33674e-01	7.19491e-01
7	-1.17384e+00	-2.18697e+00	2.31696e-01	7.70581e-01
8	-1.71532e+00	-2.48439e+00	3.01678e-02	8.19618e-01
9	-2.37924e+00	-2.68122e+00	-3.32850e-03	8.66601e-01
10	-2.91426e+00	-2.83399e+00	-3.78514e-03	9.11637e-01
15	-4.57399e+00	-3.35100e+00	-1.25733e-03	1.11264e+00
20	1.24255e-01	1.46899e+00	7.00088e-01	1.28412e+00
25	-6.80627e+00	-4.06865e+00	-8.83011e-04	1.43566e+00

Table 2. Sample of coefficients for the initial guess function $\mathscr{F}(\eta)$ (Eq. 16) for g for adiabatic wall conditions and for several edge Mach numbers. Values of g_w and $g_{\eta\eta,w}$, used to obtain $\mathcal{B}$, $\mathcal{D}$, and $\mathcal{F}$ are also listed. $g_{\eta,w}$ values are omitted since $g_{\eta,w} = 0$ for adiabatic conditions.

M_e	$\mathcal{A}$	$\mathcal{C}$	$\mathcal{E}$	g_w	$g_{\eta\eta,w}$
1	4.00238e-02	7.62938e-02	5.21708e-01	9.72390e-01	2.31501e-02
2	3.86102e-03	-1.35885e-01	5.71351e-01	9.25487e-01	7.03919e-02
3	2.37842e-03	-2.61074e-01	5.59809e-01	8.90527e-01	1.21084e-01
4	-1.02949e-01	-8.57249e-01	5.06635e-01	8.68205e-01	1.71673e-01
5	-3.53516e-01	-1.42533e+00	4.20244e-01	8.53808e-01	2.22184e-01
6	-7.14969e-01	-1.84294e+00	3.33674e-01	8.44094e-01	2.72722e-01
7	-1.17384e+00	-2.18697e+00	2.31696e-01	8.37231e-01	3.23289e-01
8	-1.71532e+00	-2.48439e+00	3.01678e-02	8.32186e-01	3.73857e-01
9	-2.37924e+00	-2.68122e+00	-3.32850e-03	8.28353e-01	4.24401e-01
10	-2.91426e+00	-2.83399e+00	-3.78514e-03	8.25358e-01	4.74904e-01
15	-4.57399e+00	-3.35100e+00	-1.25733e-03	8.16894e-01	7.26630e-01
20	1.24255e-01	1.46899e+00	7.00088e-01	8.13037e-01	9.77168e-01
25	-6.80627e+00	-4.06865e+00	-8.83011e-04	8.10866e-01	1.22686e+00

A difference between the codes lies in their perturbation boundary conditions. VESTA and the TU Delft code both use the wall-normal momentum equation as a compatibility condition, and a freestream Dirichlet condition for all quantities except $\tilde{p}$ (enforced through the same compatibility condition evaluated in the freestream).[18,23] On the other hand, EPIC uses the continuity equation as a compatibility condition and freestream Neumann conditions on all quantities ($\mathrm{d}\tilde{q}/\mathrm{d}y|_{y=y_{\max}}$).[22,24,35] These differences, however, are expected to have no significant effect in the stability results.

To establish a reasonable verification with EPIC, the stability problem is solved using the FD-q library[36,37] in VESTA, kindly provided by Dr. Hermanns. By using order $q = 4$, it yields comparable results to the scheme used in EPIC. Moreover, the deployment of the FD-q library allows comparing the performance of the higher order FD-q method with respect to the Chebyshev collocation method. In the remainder, 'FD-4', 'FD-8' and 'FD-10' will specifically denote the fourth-, eighth- and tenth-order FD-q schemes. They are not to be confused with a regular finite-difference scheme.

IV. Basic-state results

The current results are generated with the aim of providing a benchmark. To that end, it is very important to specify the thermodynamic reference variables. By carefully scrutinizing the literature, in fact, it was observed that many references do not provide such information completely, while small changes in the parameters can yield large differences in the results, *also in the essentially incompressible case* $\mathrm{M} \to 0$. The parameters that are fixed among all considered cases are given in table 3; the shown precision is used as the input exactly.

Table 3. Fixed thermodynamic reference and η-grid parameters

Pr	γ	$c_p\,(\mathrm{J/(kg\,K)})$	$\overline{\mu}_{\mathrm{ref}}\,(\mathrm{kg/(m\,s)})$	$\overline{T}_{\mathrm{ref}}\,(\mathrm{K})$	$S\,(\mathrm{K})$	η_i	$\eta_{\max}$	$\tilde{N}_{\text{FD-4}}$
0.70	1.4	1004.5	1.716×10^{-5}	273.15	110.6	6	100	500

As mentioned, the Illingworth transformation (3) factors the dilational effect of the density in the boundary layer. Therefore the boundary-layer thickness is practically invariant in the η-coordinate. For this reason, next to the thermodynamic reference values, also the values of the Malik mapping parameters, η_i and $\eta_{\max}$ are fixed and reported in this table. Note that fixing these parameters implies that the corresponding values of y_i and $y_{\max}$ change from case to case.

IV.A. Case description

A broad range of cases is investigated. For the incompressible flow regime ($\mathrm{M} = 10^{-3}$), the CrossFlow (CF) and Tollmien-Schlichting (TS) instabilities are considered. For higher sub- and supersonic Mach numbers ($\mathrm{M} = 0.8$ and 2.5), the representative oblique (first) Mack mode (M1) are inspected. The oblique nature of the latter modes is encoded in the non-zero spanwise wavenumber, $\beta \neq 0$. Finally, the second Mack mode (M2) is considered in the hypersonic ($\mathrm{M} = 10$) case. In table 4, the case-specific parameters are detailed for representative cases, the cases are numbered I through V as indicated. Studies of the CF instability case on self-similar boundary-layer profiles are very scarcely reported in the literature (to sufficient detail); which obstructed establishing external verification. For that reason, the CF case is considered in the incompressible flow regime only in this paper.

The local Blasius length is chosen as the reference length scale:

$$\ell = \sqrt{\frac{\overline{\mu}_e x}{\overline{\rho}_e \overline{Q}_e}} = \frac{\mathrm{Re}}{\mathrm{Re}_1}, \tag{17}$$

where Re_1 denotes the unit Reynolds number and $\mathrm{Re} \equiv \ell \mathrm{Re}_1$. Note that, in the limit $M \to 0$, this length scale differs from that associated to the Illingworth transformation (3) by a factor $\sqrt{2}$. The used velocity scale is:

$$\overline{Q}_e = \sqrt{\overline{u}_e^2 + \overline{w}_0^2}, \tag{18}$$

i.e. the effective inviscid flow speed. The sweep angle Λ is defined such that: $\overline{u}_e = \overline{Q}_e \cos\Lambda$ and $\overline{w}_e = \overline{Q}_e \sin\Lambda$.

Table 4. Case-specific parameters

	M	type	$\Lambda\,(^\circ)$	β_H	Re_1	$\overline{T}_e\,(\mathrm{K})$	$\overline{T}_w\,(\mathrm{K})$	Re	$\omega\,(\overline{Q}_e/\ell)$	$\beta\,(1/\ell)$	$\tilde{N}_{\mathrm{Cheb}}$
I	10^{-3}	CF	45	0.2	$1.0\cdot10^7$	220	220	$1000\sqrt{2}$	0	$\pi\sqrt{2}/15$	150
II	10^{-3}	TS	0	0	$5.8\cdot10^2$	300	adiab.	580	0.06	0	150
III	0.8	M1	0	0	$2.0\cdot10^3$	215	adiab.	580	0.04	0.1	150
IV	2.5	M1	0	0	$5.0\cdot10^6$	600/4.05	adiab.	3000	0.04	0.1	200
V	10.0	M2	0	0	$9.8425\cdot10^6$	278	adiab.	2000	0.075	0	500

Representative TS and Mack modes are unstable in zero sweep and zero pressure gradient circumstances, so $\Lambda = \beta_H = 0$ for these cases (rendering $\overline{Q}_e = \overline{u}_e$). Furthermore, an adiabatic wall is considered.

For a CF instability to exist, the boundary layer must display a crossflow component. Such a component is naturally established if the inviscid flow and the pressure gradient are not aligned. The skin friction points in the same direction of the pressure gradient to establish the steady flow and is thus also not aligned with the inviscid flow. In turn, the component of the skin friction orthogonal to the inviscid flow direction can only be manifested by a flow component in that direction: the crossflow component. A maximal crossflow component is achieved for $\Lambda = 45^\circ$. Furthermore, a favorable pressure gradient is considered, $\beta_H > 0$, which is representative of the neighborhood of the leading edge of an airfoil. In this case, an iso-thermal wall is considered.

IV.B. Grid convergence

System (5) is solved with $\overline{N}$ nodes, and to accurately assess the convergence characteristics, the following technique is used to evaluate the errors. Given a test grid with a particular number $\overline{N}$ of nodes, a finer auxiliary grid was generated with $2\overline{N} - 1$ nodes. The solutions on the test and auxiliary grids are here referred to as the test and auxiliary solutions, respectively. The auxiliary grid contains nodes at exactly the same location as the test grid, while one additional node is added in between every consecutive pair of nodes of the test grid. That is, the auxiliary solution at nodes with an odd index can be directly compared with the test solution on the test grid, without interpolation. The corresponding error is expressed as $|\epsilon(\overline{q}_{2N-1}, \overline{q}_N)|_\infty$; evaluating the ∞-norm of the difference in the variable is evaluated divided by its maximal absolute magnitude evaluated at the auxiliary grid. In the context of this section, the variable $f_{\eta\eta}$ is chosen for $\overline{q}$, representative of the shear in the flow. The presented data-points always correspond to the number of nodes $\overline{N}$ of the test grid.

As $\overline{N}$ increases linearly, the spectral convergence characteristics of the collocation scheme must result in an exponential decrease of the magnitude of the error. The achievement of this trend is demonstrated for all considered cases in figure 1, which verifies the spectral accuracy of the solver. The figure moreover indicates that all velocity profiles, despite the large differences in the conditions, are converged for $\overline{N} \geqslant 90$. For this reason, $\overline{N} = 100$ is used for the profiles that are used as the input for the stability problem. The inverse of the slope of the line connecting the errors at $\overline{N} = 30$ and 90 is calculated for case IV, which indicates that the error decreases by an order of magnitude if 6 additional nodes are used.

IV.C. Parameter accuracy

The representative base flow profiles corresponding to the cases in table 4 are illustrated in figure 9. It is argued that, in order to yield identical stability results, one must be able to match the basic-state profiles up to the derivative level(s). Therefore, next to the profiles themselves, also the first and second derivative profiles are given. It should be noted that the temperature profiles in figures 9 (V(a),V(b),V(c)) are scaled by a factor 10; this was required to have a reasonable view of the profiles related to the velocity. The largest plotted value of y/ℓ is y_i/ℓ (see table 6).

To indicate the accuracy of the solutions in a different way, the boundary-layer integral parameters are evaluated. In particular, the displacement thickness, δ^*, the momentum thickness, θ^*, shape factor, H^*, the

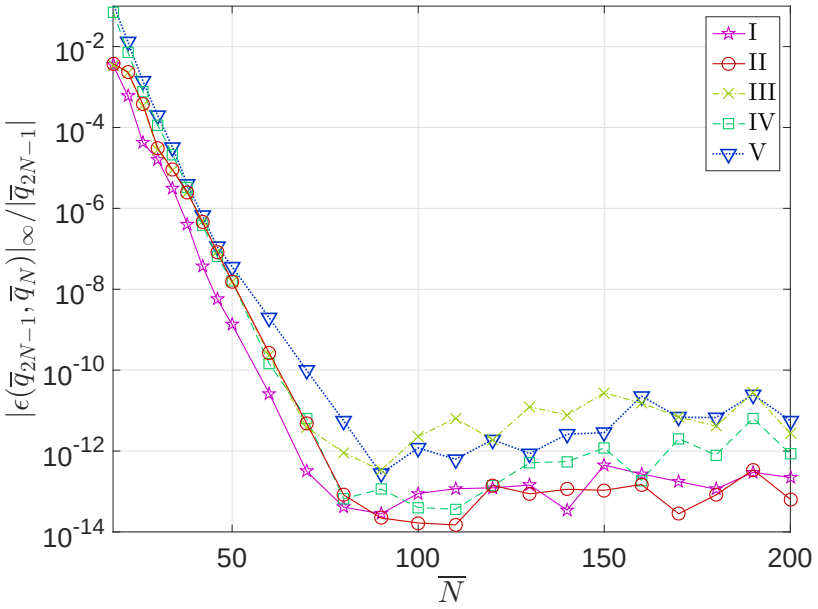

Figure 1. Relative error versus the number of nodes for all cases in table 4.

energy thickness, δ_e^* and the enthalpy thickness, δ_h^*, defined as:

$$\delta^* = \int_0^\infty \left(1 - \frac{\overline{\rho u}}{\overline{\rho}_e \overline{u}_e}\right) \mathrm{d}y, \qquad \theta^* = \int_0^\infty \frac{\overline{\rho u}}{\overline{\rho}_e \overline{u}_e}\left(1 - \frac{\overline{u}}{\overline{u}_e}\right) \mathrm{d}y, \qquad \mathrm{H}^* = \delta^*/\theta^*,$$
$$\delta_e^* = \int_0^\infty \frac{\overline{\rho u}}{\overline{\rho}_e \overline{u}_e}\left(1 - \frac{\overline{u}^2}{\overline{u}_e^2}\right) \mathrm{d}y, \qquad \delta_h^* = \int_0^\infty \frac{\overline{\rho u}}{\overline{\rho}_e \overline{u}_e}\frac{\overline{T} - \overline{T}_e}{\overline{T}_w - \overline{T}_e} \mathrm{d}y, \tag{19}$$

where the integrals are evaluated with the integration matrices, see Appendix A. In addition to the integral parameters, the wall values of selected profiles are considered. For the cases considered, many values evaluate to zero and therefore are not of particular interest. In the perspective of the non-zero sweep for case I, note that the integral parameters evaluated at the wall are scaled with $\overline{u}_e$ instead of $\overline{Q}_e$, the same applies to the non-dimensionalization of the wall values. Note that δ_h^* cannot be determined numerically for case I, where $\overline{T}_w = \overline{T}_e$.

The resulting values of the integral parameters are reported in table 5, whereas the velocity gradient values and mapping parameters, y_i and $y_{\max}$, are reported in table 6. The reported digits are found to be significant by checking the matching digits for $\overline{N} = 100$ and 200, where $\overline{N}$ represents the number of collocation nodes. I.e. values are not rounded. Due to the further use of the values of y_i and $y_{\max}$, they are reported to their full extent corresponding to the $\overline{N} = 100$ case; the red digits were found to be non-significant in relation to the $\overline{N} = 200$ case.

Table 5. Integral parameters.

	δ^*/ℓ	θ^*/ℓ	$\mathrm{H}^* = \delta^*/\theta^*$	δ_e^*/ℓ	δ_h^*/ℓ
I	1.39181039	0.577324959	2.410792003	0.920585142	-
II	1.72078806681	0.66411466327	2.5911008474	1.0443754620	1.24967659
III	1.98658629736	0.66000141833	3.00997277002	1.03845829284	1.243088604
IV	4.2571098871	0.63906449395	6.6614714593	1.0085588870	1.209953346
V	27.043037097	0.418786146490	64.574813001	0.67454497161	0.8245472549

A good illustration of the method's accuracy with respect to the sensitivity to changes in the temperature is provided by the cases I and II. Both involve a very small Mach number, but are different in that an

Table 6. First $\overline{u}$ derivative at the wall and grid parameters (red digits are non-significant, specific for $\overline{N} = 100$).

	$(\mathrm{d}\overline{u}/\mathrm{d}y)_w(\ell/\overline{u}_e)$	y_i/ℓ	$y_{\max}/\ell$
I	0.485576015007	8.4852814593205892	141.42135632239169
II	0.3320572889362	8.4852818153039173	141.42135667837809
III	0.3033648852327	8.7653732078111020	141.70145010884812
IV	0.174839002926	11.110121719743736	144.04621197745197
V	0.036774705710	34.532948309235067	167.46903831963368

Table 7. Extra values evaluated at the wall for cases I (iso-thermal wall) and II (adiabatic wall).

	$(\mathrm{d}^2\overline{u}/\mathrm{d}y^2)_w(\ell^2/\overline{u}_e)$	$\overline{T}_w/\overline{T}_e$	$(\mathrm{d}\overline{T}/\mathrm{d}y)_w(\ell/\overline{T}_e)$	$(\mathrm{d}^2\overline{T}/\mathrm{d}y^2)_w(\ell^2/\overline{T}_e)$
I	-0.10000002172	1.0000000000000000	$5.362 \cdot 10^{-8}$	$-5 \cdot 10^{-8}$
II	$0 \pm 3 \cdot 10^{-13}$	1.000000167143317	$0 \pm 8 \cdot 10^{-14}$	$0 \pm 3 \cdot 10^{-8}$

isothermal and adiabatic condition for the temperature is considered. Note that, for case II, $\overline{T}_w - \overline{T}_e$ is very small, but non-zero. Using the approximation for the adiabatic wall temperature (see equations (7-35) and (7-37a) of White[21]):

$$\frac{\overline{T}_{\mathrm{ad}}}{\overline{T}_e} = 1 + r\frac{\gamma - 1}{2}\mathrm{M}^2, \qquad \text{where: } r \approx \sqrt{\mathrm{Pr}}, \tag{20}$$

yields $\overline{T}_{\mathrm{ad}}/\overline{T}_e = 1 + 1.673 \cdot 10^{-7}$. In table 7, the computed value of $\overline{T}_w/\overline{T}_e$ is reported, which illustrates that the former approximation yields 3 significant digits. Note that $\overline{T}_w/\overline{T}_e$ is identically equal to 1 for case I, also reported in table 7. This is a non-trivial result, because the primitive solution variable corresponding to g is the total enthalpy, $\overline{H}$, whose wall value $\overline{H}_w/\overline{H}_e$ is non-zero.

Due to the very small temperature change, the scaling of the boundary layer is affected to an equally small extent. This change is best represented by the values of y_i and $y_{\max}$ in table 6, both correspond to $\eta_i = 6$ and $\eta_{\max} = 100$, respectively. Just like the temperature difference, these values change in the eighth significant digit. The collocation approach is capable of resolving this difference up to several orders of magnitude, as indicated with the underlined digits in table 6.

IV.D. Interpolation errors

In solving the stability problem, usually a different grid is used than that corresponding to the base flow profiles. The spectral computational power of the method has the downside that the used grid is relatively sparse, so caution should be exercised when interpolating. For that reason, the influence of interpolating the solutions is tested. Specifically, the solution on the test grid is interpolated onto the auxiliary grid with different methods (linear, spline or GICM interpolation), where it is compared to the auxiliary solution. The exact errors defined in the previous section are referred to as the 'no interp.' errors in what follows. The differences with these 'no-interp.' errors directly indicate the interpolation error; if the errors overlap, the interpolation error is negligible. In this case, the variable g_η is considered corresponding to case IV in table 4, specifically. The compressibility effects yield a large distortion of the y_2- versus the y_1-grid in this case.

The comparison of the errors are presented in figure 2. Clearly 'linear' and 'spline' interpolation yield a large error with respect to the 'no-interp.' case. While the solution is completely converged for $\overline{N} = 90$, these methods introduce errors of $O(10^{-6})$ and $O(10^{-3})$, respectively. When performing GICM interpolation, a remarkable agreement is found between the interpolated and auxiliary solution, rendering the GICM interpolation curve to lie on top of the 'no interp.' errors. It is hence deduced that, despite the sparsity of the grid used, GICM interpolation is exact to numerical precision.

V. Stability results

Given the converged boundary-layer solutions, the stability problem can be considered. For every case in table 4, a single evaluation of the stability problem is performed for α, given real values of ω and β as the

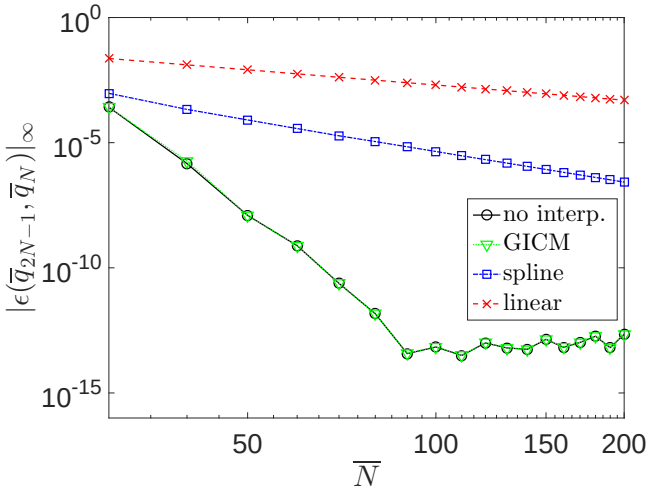

Figure 2. Grid convergence for case IV while interpolating the solution from the grid with $\overline{N}$ nodes to the one with $2\overline{N}-1$.

input. The latter values are presented in table 4. Each case corresponds to a situation where the modes are unstable. The eigenfunctions for all cases are shown in figure 10; note that the functions that are orders of magnitude smaller are scaled to allow a representative view.

V.A. Stability grid convergence

While fixing the base flow resolution to $\overline{N} = 100$, the convergence characteristics of the eigenvalues are tested by increasing the number of nodes used in the stability problem, denoted by $\tilde{N}$. In this case, the measure for the error is the absolute value of the difference in the eigenvalues with respect to the eigenvalue obtained for the largest $\tilde{N}$ considered, scaled by the magnitude of the latter value.

The resulting convergence trends are illustrated for all cases in figure 3. For the Chebyshev spectral collocation method, the errors decay exponentially with respect to $\tilde{N}$, while a fourth-order polynomial rate is attained when deploying the FD-q method with $q = 4$. A remarkable fact is that the convergence is significantly obstructed for the hypersonic case V when evaluated with the collocation method. This may be explained by the demanding shape of the eigenfunction shown in figure 10. Nevertheless, an exponential convergence rate is obtained.[k] This verifies the expected performance of both methods.

The FD-4 method results in $O(10^{-6})$ errors for the largest $\tilde{N}$ shown in figure 3. As stated by Paredes *et al.*[38] and De Tullio *et al.*,[39] the best compromise between accuracy and efficiency is acquired with FD-8 or FD-10. In figure 4, the convergence curves are shown for these approaches, applied to case IV. Consistent convergence rates are attained and a significant difference in accuracy is observed over FD-4; FD-8 and FD-10 attain the same convergence level as the spectral collocation method for $\tilde{N} \approx 420$ and 250, respectively. An interesting observation is that both methods have a smaller error than the Chebyshev collocation method for $\tilde{N} = 40$; the first data-point.

V.B. Differentiating on the base flow or stability grid

For the previously considered cases, all basic-state profiles were interpolated onto the grids corresponding tot he used stability method, including the spatial derivatives ($\mathrm{d}\overline{q}/\mathrm{d}y$ and $\mathrm{d}^2\overline{q}/\mathrm{d}y^2$). One may argue that the derivatives are most accurately represented on the grid and by the scheme (Chebyshev) with which the basic-state solution is determined in the first place. The residuals were measured using those tools after all. Another valid argument, however, is that one must provide the most accurate derivative profiles that are consistent with the stability problem, specifically. In that case, it is preferred to evaluate the derivative profiles on the grid and with the scheme associated to the stability problem instead. In fact, VESTA and the in-house code of TU Delft are usually operated according to the first methodology: differentiate first with

[k]The convergence rate for case V may be improved by considering a mapping that distributes the nodes more efficiently for this case.

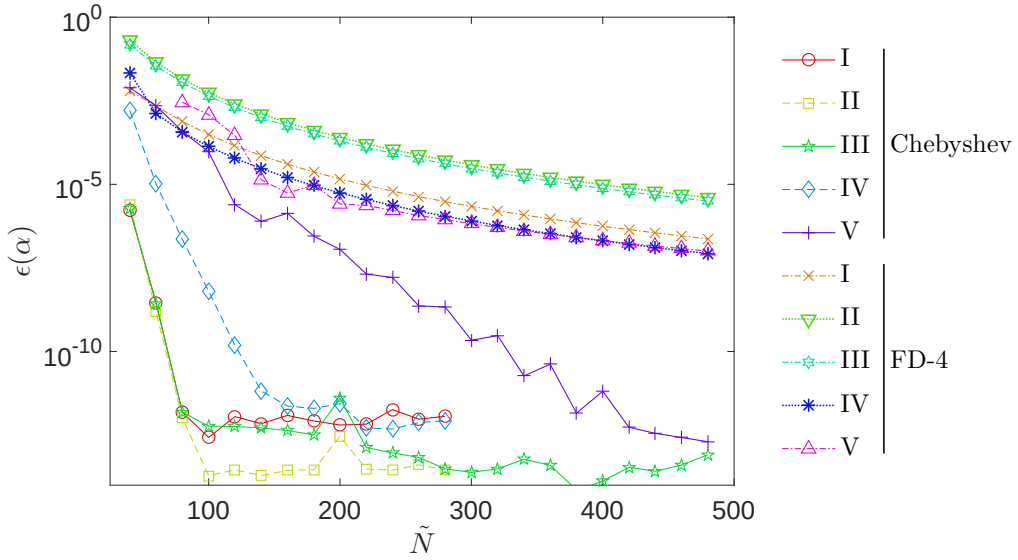

Figure 3. Eigenvalue convergence with $\tilde{N}$ for all cases in table 4, fixing $\overline{N} = 100$, using Chebyshev collocation and FD-4.

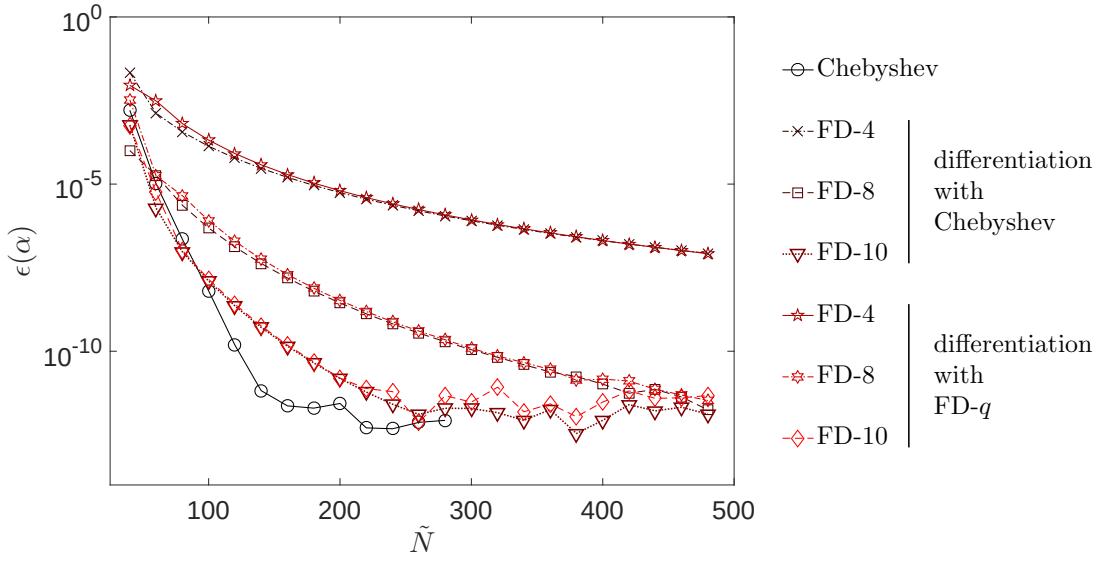

Figure 4. Eigenvalue convergence with $\tilde{N}$ for case IV, fixing $\overline{N} = 100$, using higher order FD-q methods and assessing the difference that results when differentiating the base flow profiles consistent with the base flow discretization (Chebyshev) or with the discretization of the stability problem (FD-q).

the basic-state grid and scheme and interpolate thereafter; while EPIC considers the converse methodology: interpolate the profiles first and then evaluate the derivatives consistently with the grid and scheme of the stability problem.

To test the compatibility of the results, the stability problem corresponding to case IV is evaluated with the FD-4, -8 and -10 methods, while differentiating the base flow profiles using the respective FD-q differentiation matrices. The resulting error curves are also shown in figure 4. Apart from a slight increase in the errors for small $\tilde{N}$ when differentiating with the FD-q matrices, both methods yield practically the same errors. This demonstrates that one method is not preferred over the other in the search for accurate solutions.

V.C. Base flow induced errors

The ultimate question that this study intends to answer is what accuracy is required for the base flow profiles to ensure a particular accuracy of the stability results. To approach this question, the convergence tests for increasing $\tilde{N}$ are redone while varying $\overline{N}$ as a parameter. The spectral collocation method is used for both the basic-state and stability calculations. Figure 5 a) and b) illustrates two resulting convergence trends for case IV.

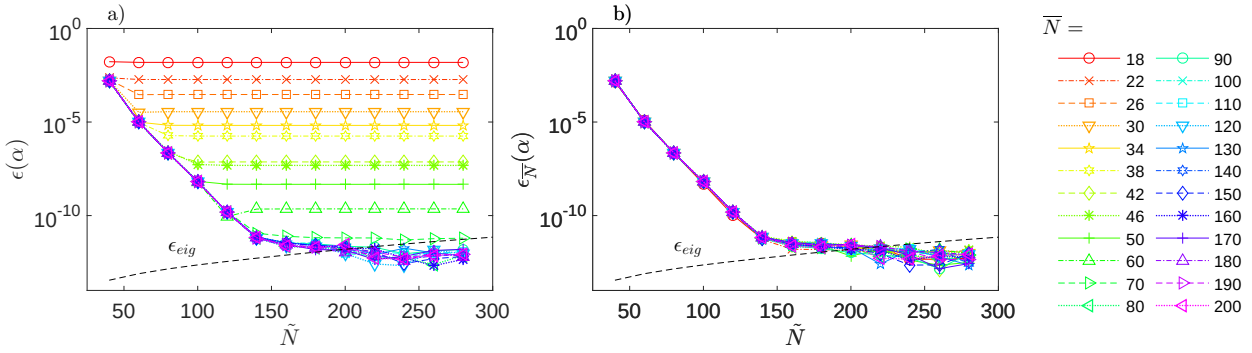

Figure 5. Convergence of the absolute eigenvalue error for case IV versus $\tilde{N}$ and treating $\overline{N}$ as a parameter. Dashed line: eigensolver error, ϵ_{eig}. In a), the error with respect to the reference solution is considered, which is converged with respect to both $\overline{N}$ and $\tilde{N}$, this error is denoted by $\epsilon(\alpha)$. In b), the error is considered with respect to the eigenvalue that results for convergence in $\tilde{N}$, but keeping $\overline{N}$ fixed, denoted by $\epsilon_{\overline{N}}(\alpha)$.

First consider figure 5 a), which displays the convergence of the results through the error measure defined before. For large enough $\overline{N}$, increasing $\tilde{N}$ results in machine-precision-accurate stability solutions. For $\tilde{N} > 170$, $\epsilon(\omega)$ decreased below ϵ_{eig}, which represents the eigensolver precision, defined as follows:[32]

$$\epsilon_{eig} = \epsilon ||A||_F, \tag{21}$$

where $||A||_F$ denotes the Frobenius norm of the left-hand-side matrix in the eigenvalue problem and ϵ is the machine precision, $2.2 \cdot 10^{-16}$ in this case. The fact that the eigenvalue error drops below this level indicates that the best possibly expected error level is reached. As before, these best possible stability solutions (converged in both $\overline{N}$ and $\tilde{N}$) are used as the reference to evaluate the errors in the eigenvalues for each case I-V. The errors corresponding to the other cases computed with the collocation method specifically, shown in figure 3, are also converged to magnitudes smaller than ϵ_{eig}. For all these cases, this convergence level is attained for $\overline{N} = 100$.

For small $\overline{N}$, as shown for case IV in particular for $\overline{N} < 80$, the error in the stability results reaches a particular plateau while increasing $\tilde{N}$. This implies that the solution approaches a different limit than the reference solution as $\tilde{N}$ is increased.

To show that indeed a particular limit is reached for each considered $\overline{N}$-value, a different error is defined. In particular, the eigenvalue difference is considered with respect to the eigenvalue that results from convergence in $\tilde{N}$ *only*, while $\overline{N}$ is kept fixed. This error is denoted by $\epsilon_{\overline{N}}(\alpha)$. Figure 5 b) shows that convergence of the stability results is attained for all considered $\overline{N}$, even for $\overline{N} = 18$.

As exemplified in figure 5 a), however, the limiting solutions are not the same for $\overline{N} < 80$. For small $\overline{N}$, errors in the base flow profiles contaminate the stability problem such that an incorrect solution is found when performing grid convergence tests for the stability problem only. This emphasizes the point made by

Reed *et al.*,[11] that the effect of the resolution of the base flow on the stability results should be checked next to the grid convergence of the stability problem itself.

Due to the access to the highly accurate reference solutions, the behavior of this hidden error can be assessed. This is done by considering the ensemble convergence trend as $\tilde{N}$ and $\overline{N}$ are varied together. The results of this study are represented by plotting the error in the base flow profiles versus the errors in the eigenvalues; $\epsilon(\overline{q})$ versus $\epsilon(\alpha)$. In essence, this plot could be used as a guide: given a demanded accuracy of the stability results on the horizontal axis, this plot shows the minimally required accuracy (or maximally allowed errors) for the base flow profiles on the vertical axis. Again, the error in the base flow profiles is determined by using the 'no-interp.' methodology, explained in §IV.D.

The resulting plots are shown in figure 6. As $\tilde{N}$ is increased, the corresponding ensemble of symbols moves to the left (as illustrated with the blue-red color shift), indicating an improvement of the stability information. For increasing $\overline{N}$, the ensemble of symbols moves downwards, indicating an improvement in the base flow accuracy; again the error is based on the variable $f_{\eta\eta}$.

As $\tilde{N}$ increases, the data-points encounter the aforementioned threshold, which lies in the neighborhood of the line corresponding to $\epsilon(\overline{q}) = \epsilon(\alpha)$ indicated with the dashed line. In fact, the maximal allowed error in the base flow profiles *lies above the line* $\epsilon(\overline{q}) = \epsilon(\alpha)$ *for nearly all cases*. These errors can be one order of magnitude larger as indicated with the solid line. So, if one would request stability data with an accuracy of $\epsilon(\alpha) = \varepsilon$, the former result implies that the required order of magnitude of the error in the base flow can be an order of magnitude larger, $\epsilon(\overline{q}) > \varepsilon$. Note that figure 6 displays the same threshold value when using the Chebyshev collocation scheme of FD-4 to compute the stability results. This indicates that this threshold is independent of the stability method. These results are expected to be dependent on the numerical scheme used for the basic-state solution (Chebyshev spectral collocation).

To conclude, this shows that errors in the base flow (derivative!) profiles do not necessarily yield errors in the stability results of the same magnitude. Theofilis[40] states in this light that:

> if numerical residuals exist in the basic state (at $O(1)$) they will act as forcing terms in the $O(\varepsilon)$ disturbance equations and result in erroneous instability predictions.

The latter results show that this, in a sense, is true. However, the errors in the stability results do not necessarily have the same order of magnitude as the errors in the base flow; they are possibly one order of magnitude smaller.

V.D. Real versus imaginary part

As mentioned, the error measure that has been used up to this point involves the absolute value of the difference of the eigenvalues. This measure does not discriminate between the errors in the real and imaginary parts of the eigenvalue. Given the broad range of cases, an insight can be gained into the extent in which the real and imaginary parts individually contribute to the error that is representative for stability calculations in general.

To this end, figure 7 plots the relative error in the real part versus that in the imaginary part, based on the data shown in figure 6. The data-points cluster around the dashed line, which corresponds to equal contributions, $\epsilon(\alpha_i) = \epsilon(\alpha_r)$. This implies that the error in the real and imaginary part of the eigenvalue have the same order of magnitude. This implies that the trajectory of the eigenvalue through the complex plane is bounded to a particular ellipse in the complex plane, when increasing $\tilde{N}$. A linear fit is performed on the data-points to assess the overall trend, which resulted in the proportionality relation: $\epsilon(\alpha_i) \sim \epsilon(\alpha_r)^{0.95}$. The fit is shown as the solid line in figure 7, which lies below the dashed line. This indicates that the error in the eigenvalue tends to be dominated by the contribution of the error due to the real part.

V.E. Benchmark results

Having demonstrated that the solutions are converged with respect to both resolutions of the base flow and the stability problem, the results are now presented as a benchmark for code verification.

The resolution of the base flow profiles is fixed to $\overline{N} = 100$. The stability codes that deploy the Chebyshev collocation method, VESTA and the in-house stability code of TU Delft, use $\tilde{N} = 150$ for all cases except cases IV and V. In those cases, $\tilde{N} = 200$ and 500 were considered, respectively. These numbers are also reported in table 4.

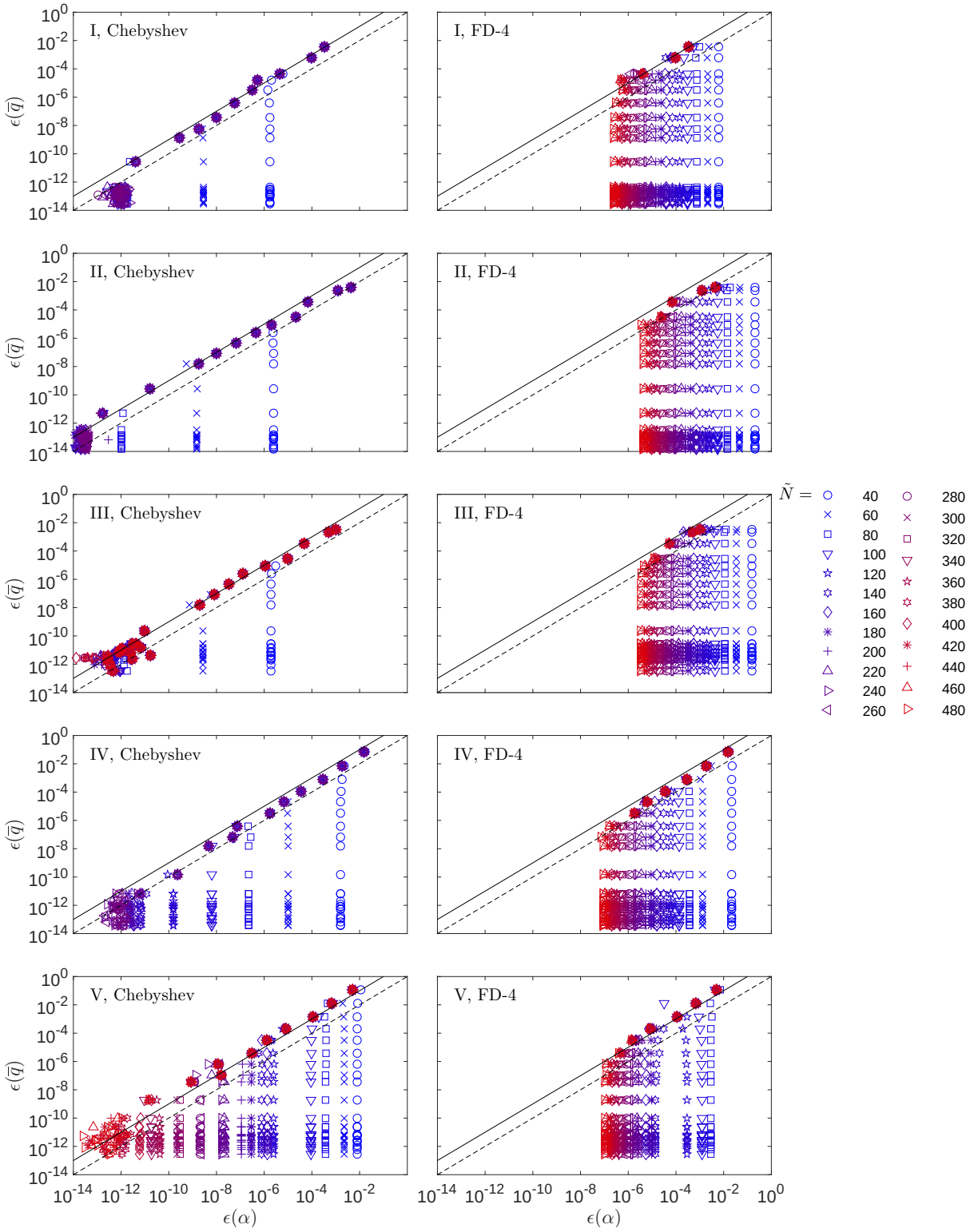

Figure 6. Errors in the base flow versus errors in the eigenvalues for all cases in table 4. Dashed line: $\epsilon(\overline{q}) = \epsilon(\alpha)$. Solid line: $\epsilon(\overline{q}) = 10\epsilon(\alpha)$. Both $\epsilon(\overline{q})$ and $\epsilon(\alpha)$ are *relative* errors; $\epsilon(\alpha)$ is computed versus the 'best' reference result, while $\epsilon(\overline{q})$ performs the 'no-interp.' method: comparing the solution computed with $\overline{N}$ nodes to the auxiliary solution on the grid with $2\overline{N} - 1$ nodes.

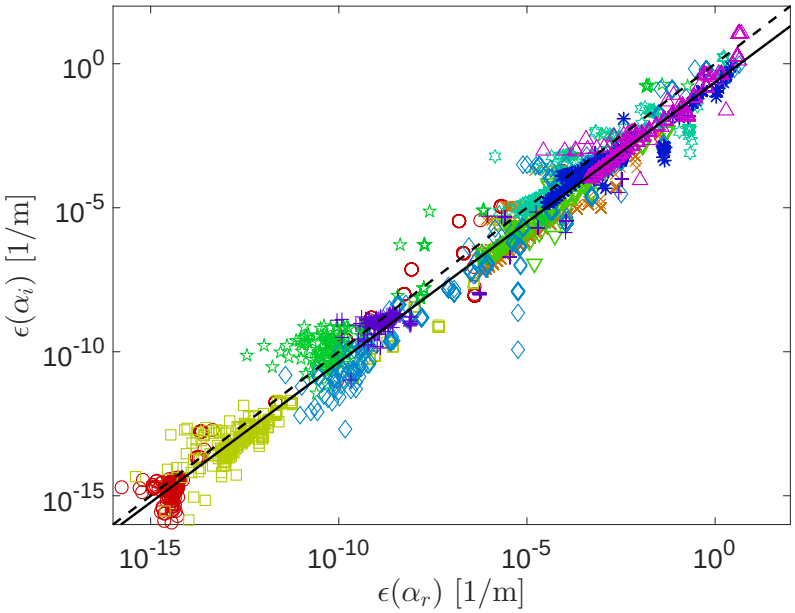

Figure 7. Contribution of the real and imaginary part to the total error in the eigenvalue for all convergence data presented in figure 3. Dashed line: $\epsilon(\alpha_i) = \epsilon(\alpha_r)$ (correlation coefficient with respect to this line equals: 0.941). Solid line: $\epsilon(\alpha_i) \sim \epsilon(\alpha_r)^{0.95}$, fitting the $\epsilon(\alpha_i)$- to the $\epsilon(\alpha_r)$-values (correlation coefficient for this line: 0.969).

The comparison of the results generated with VESTA and the TU Delft code is shown in table 8. Next to the real and imaginary part of α for the different codes, the relative errors and the values of ϵ_{eig} are tabulated and the first digit that displays a mismatch is underlined for every case. Due to the spectral convergence characteristics of the used numerical method the results match up to 13 significant digits. Moreover, the match is very close to the theoretical limit indicated by ϵ_{eig}. For case III it is, in fact, exceeded. This yields a successful completion of the cross-verification of VESTA and the in-house stability code of TU Delft.

For comparison purposes, purely incompressible (i.e. M = 0) stability calculations are performed with the TU Delft code for cases I and II. The use of the compressible and incompressible code is indicated with the superscript c and i, respectively, in table 8. Due to the very small Mach number for cases I and II (M = 10^{-3}), a very small difference in the eigenvalues is expected. Indeed, for case I (CF) and II (TS), this difference turns out to be of $O(10^{-10})$ and $O(10^{-7})$, respectively. The extreme accuracy provided by the Chebyshev collocation method allows resolving this difference to several orders of magnitude (at least 2 for case I (CF) and 4 for case II (TS)). This is a demonstration of that very small changes in the stability data due to very small changes in the base flow can be accurately captured.

EPIC uses a fourth-order finite-difference scheme for the stability calculations by standard and is executed using $\tilde{N} = 500$ for all cases. By deploying the FD-4 method for the stability calculations with VESTA, the calculations performed with EPIC can be fairly evaluated.

The comparison of the results generated with VESTA and EPIC is tabulated in table 9. Again, the relative errors for the real and imaginary parts are reported next to the real and imaginary parts themselves. The digits provided by VESTA with FD-4 that differ from the numbers reported in table 8 are colored red. The digit on which the result calculated with EPIC differs from that of VESTA is always located within second places from the red digits. Furthermore, it was observed in figure 4 that errors of $O(10^{-7})$ to $O(10^{-5})$ could be expected due to the convergence characteristics of the fourth-order (FD-4) finite differences. All relative errors presented in table 8 are within this range, so the verification can be declared to be successful.

VI. Conclusion

Stability results are notoriously sensitive to changes in the base flow. In order to securely assess the dependency of the stability information on minute differences in the base flow, the best numerical base flow solutions must be used.

Table 8. Eigenvalues obtained using Chebyshev spectral collocation. First mismatching digits are underlined.

	solver	α_r (rad/m)	$\epsilon(\alpha_r)$	α_i (rad/m)	$\epsilon(\alpha_i)$	ϵ_{eig}
I	VESTA	$-1.96373280971733 \cdot 10^3$	$6.2 \cdot 10^{-12}$	$-3.51018997117582 \cdot 10^1$	$1.1 \cdot 10^{-11}$	$7.7 \cdot 10^{-13}$
	TUD^c	$-1.96373280972951 \cdot 10^3$	$8.6 \cdot 10^{-10}$	$-3.51018997331673 \cdot 10^1$	$2.8 \cdot 10^{-8}$	$7.7 \cdot 10^{-13}$
	TUD^i	$-1.96373280803897 \cdot 10^3$		$-3.51019007106470 \cdot 10^1$		$6.8 \cdot 10^{-13}$
II	VESTA	$1.67060311770109 \cdot 10^{-1}$	$4.4 \cdot 10^{-12}$	$-4.079840183775 \cdot 10^{-3}$	$2.5 \cdot 10^{-12}$	$2.0 \cdot 10^{-12}$
	TUD^c	$1.67060311770840 \cdot 10^{-1}$	$1.8 \cdot 10^{-7}$	$-4.079840183356 \cdot 10^{-3}$	$9.8 \cdot 10^{-7}$	$2.0 \cdot 10^{-12}$
	TUD^i	$1.67060341298808 \cdot 10^{-1}$		$-4.079844179169 \cdot 10^{-3}$		$1.5 \cdot 10^{-12}$
III	VESTA	$3.41664315531627 \cdot 10^{-1}$	$5.1 \cdot 10^{-13}$	$-7.539434881703 \cdot 10^{-3}$	$4.1 \cdot 10^{-13}$	$1.6 \cdot 10^{-12}$
	TUD	$3.41664315531800 \cdot 10^{-1}$		$-7.539434881563 \cdot 10^{-3}$		$2.0 \cdot 10^{-12}$
IV	VESTA	$1.07402614379007 \cdot 10^2$	$9.4 \cdot 10^{-13}$	$-1.03977656691188 \cdot 10^0$	$5.1 \cdot 10^{-12}$	$2.0 \cdot 10^{-12}$
	TUD	$1.07402614379108 \cdot 10^2$		$-1.03977656636347 \cdot 10^0$		$6.2 \cdot 10^{-13}$
V	VESTA	$3.86915377502036 \cdot 10^2$	$4.7 \cdot 10^{-12}$	$-7.98862348202598 \cdot 10^0$	$3.5 \cdot 10^{-12}$	$2.9 \cdot 10^{-11}$
	TUD	$3.86915377503853 \cdot 10^2$		$-7.98862348069057 \cdot 10^0$		$1.7 \cdot 10^{-11}$

Table 9. Eigenvalues obtained using fourth-order finite differences. First mismatching digits are underlined; digits corresponding to VESTA that do not match with table 8 are colored red.

	solver	α_r (rad/m)	$\epsilon(\alpha_r)$	α_i (rad/m)	$\epsilon(\alpha_i)$
I	VESTA	$-1.9637324 \cdot 10^3$	$1.5 \cdot 10^{-5}$	$-3.5101810 \cdot 10^1$	$3.0 \cdot 10^{-5}$
	EPIC	$-1.9637621 \cdot 10^3$		$-3.5100744 \cdot 10^1$	
II	VESTA	$1.6705982 \cdot 10^{-1}$	$9.0 \cdot 10^{-6}$	$-4.0798177 \cdot 10^{-3}$	$4.1 \cdot 10^{-6}$
	EPIC	$1.6705832 \cdot 10^{-1}$		$-4.0798009 \cdot 10^{-3}$	
III	VESTA	$3.4166345 \cdot 10^{-1}$	$8.5 \cdot 10^{-6}$	$-7.5392515 \cdot 10^{-3}$	$5.1 \cdot 10^{-5}$
	EPIC	$3.4166054 \cdot 10^{-1}$		$-7.5388700 \cdot 10^{-3}$	
IV	VESTA	$1.0740260 \cdot 10^2$	$3.5 \cdot 10^{-7}$	$-1.0397715 \cdot 10^0$	$8.0 \cdot 10^{-6}$
	EPIC	$1.0740257 \cdot 10^2$		$-1.0397798 \cdot 10^0$	
V	VESTA	$3.8691534 \cdot 10^2$	$2.7 \cdot 10^{-7}$	$-7.9886366 \cdot 10^0$	$5.7 \cdot 10^{-5}$
	EPIC	$3.8691524 \cdot 10^2$		$-7.9890911 \cdot 10^0$	

To this end, this paper presents DEKAF (Digits by Ethan, Koen, Alex and Fernando), a code using the Chebyshev spectral collocation method to discretize the compressible variant of the Falkner-Skan-Cooke equations for self-similar boundary layers. The system of equations is solved with Newton-Raphson iteration. Due to the high numerical order of the collocation method, the self-similar solutions are obtained up to machine precision for a broad range of Mach numbers.

Due to the high sparsity of the collocation node grid for the basic state, having to interpolate onto the grid used for the stability problem deteriorates the accuracy of the solutions to a significant extent if conventional interpolation methods are used. This problem is solved by introducing a dedicated interpolation method referred to as GICM (the Groot-Illingworth-Chebyshev-Malik interpolation method). This routine resolves the complication introduced by the self-similarity transformation and grid mappings, so that the optimal interpolation characteristics of the Chebyshev collocation method equipping Chebyshev Gauss-Lobatto nodes can be accessed. The performance of GICM is found to be exact to numerical precision.

Given the highly accurate base flow solutions, the convergence characteristics of the stability problem are assessed. Next to the stability grid convergence, also the effect of errors in the base flow profiles are assessed. The combination of the Chebyshev discretization of the base flow profiles and GICM allows obtaining highly accurate stability solutions for all Mach numbers. By using machine-precision resolution for both the basic-

state and stability problem, the best possible stability solutions in double-precision arithmetic are found. These benchmark solutions are cross-verified by using VESTA, EPIC and the in-house stability code of TU Delft.

In agreement with Paredes *et al.*,[37] the numerical convergence of the FD-10 method is found to be very close to that of the Chebyshev collocation method. Moreover, computing the spatial derivatives of the basic-state quantities with the numerical scheme used for the basic state (Chebyshev collocation) or with the FD-q schemes, yielded practically the same eigenvalue accuracy.

By varying both the resolution of the basic-state and stability problems, it is assessed whether a criterion exists that prescribes the required accuracy of the basic state to ensure a given accuracy of the stability results. For low resolutions of the basic state, the basic-state inaccuracies contaminate the stability solution. Therefore, convergence to an incorrect solution results when resolving the stability grid alone—while keeping the basic-state resolution fixed. This effect was quantified by comparing the solutions with different basic-state and stability grid resolutions to the benchmark solutions, for a variety of numerical techniques, flow regimes and instability mechanisms.

Surprisingly, it is found for all considered cases that, given a representative error in the basic state of ε, the relative effect on the stability results is consistently smaller than ε. This trend is found to be preserved for the entire range of considered basic-state resolutions and the numerical discretization of the stability problems (Chebyshev collocation and FD-4 are used). Instances are found where the effect on the stability results is an order of magnitude smaller than ε.

Conversely, this demonstrates that converged stability results can be attained, now denoting the requested error in the stability results by ε, from base flow profiles that are contaminated by an error of possibly an order of magnitude larger, i.e. 10ε. Errors in the base flow can yield changes in the stability results that are an order of magnitude smaller.

Appendices

A. Procedure for obtaining spectral-accuracy integration matrices

An integration is required to convert the self-similarity coordinate, η, back into the spatial coordinate, y. In light of the pursued accuracy, this is performed with an integration matrix, I, that is the numerical inverse of the differentiation matrix D delivered by the functions by Weidemann & Reddy,[16] for a CGL grid with N collocation nodes.

This is done in three steps, see figure 8. Specifically the case is illustrated for the integral with respect to the $y = 0$ coordinate corresponding to the wall. In the first step, the bottom row in the differentiation matrix D is replaced by the corresponding row of the identity matrix. That is:

$$\tilde{D}_{N,i} = \delta_{Ni} \qquad \text{for: } i = 1, \ldots, N, \tag{22}$$

where δ_{ji} is the Kronecker delta. This annihilates the inherent null-space of the differentiation matrix, which allows inverting the resulting matrix numerically, as a second step. In the third step, a row of ones is subtracted from the bottom row. In terms of the symbols introduced in figure 8, the elements $\tilde{I}_{N,i}$, with i ranging from 1 to N, are replaced by the values $I_{N,i}$, where:

$$I_{N,i} = \tilde{I}_{N,i} - 1 \qquad \text{for: } i = 1, \ldots, N. \tag{23}$$

This ensures that the integral evaluates to zero at the wall boundary.

A similar procedure can be performed on the top row to result in a matrix that integrates with respect to the freestream boundary. Similarly, one can place the reference point at any of the interior collocation points.

The spectral accuracy of the resulting integration matrix was confirmed by applying it to elementary functions.

References

[1] Van Ingen, J. L., "A suggested semi-empirical method for the calculation of the boundary layer transition region," Vth-74, Delft University of Technology, The Netherlands, 1956.

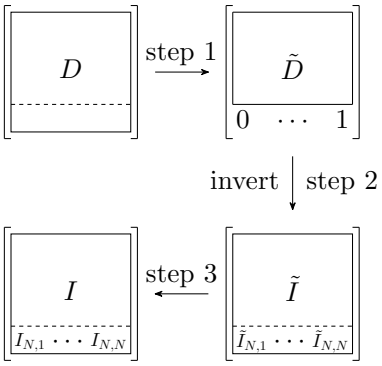

Figure 8. Illustration of the procedure for obtaining the integration matrix I from the differentiation matrix D from the Weidemann & Reddy toolsuite.[16]

[2]Smith, A. and Gamberoni, N., "Transition, pressure gradient and stability theory," *Aircraft Co., Report No. ES 26 388, El Segundo, CA*, 1956.

[3]Schrauf, G., "Industrial view on transition prediction," *Recent Results in Laminar-Turbulent Transition*, Springer, 2004, pp. 111–122.

[4]Crouch, J., "Modeling transition physics for laminar flow control," *AIAA Paper, 3832-2008*, 2008.

[5]Pinna, F. and Groot, K. J., "Automatic derivation of stability equations in arbitrary coordinates and different flow regimes," *44th AIAA Fluid Dynamics Conference, Atlanta, GA*, 2014.

[6]Ehrenstein, U. and Gallaire, F., "On two-dimensional temporal modes in spatially evolving open flows: the flat-plate boundary layer," *Journal of Fluid Mechanics*, Vol. 536, 2005, pp. 209–218.

[7]Alizard, F. and Robinet, J. C., "Spatially convective global modes in a boundary layer," *Physics of Fluids*, Vol. 19, No. 11, 2007.

[8]Åkervik, E., Ehrenstein, U., Gallaire, F., and Henningson, D. S., "Global two-dimensional stability measures of the flat plate boundary-layer flow," *European Journal of Mechanics B/Fluids*, Vol. 27, No. 5, 2008, pp. 501–513.

[9]Rodríguez, D. A., *Global Instability of Laminar Separation Bubbles*, Ph.D. thesis, Universidad Politécnica de Madrid, 2010.

[10]Rodríguez, D. A., Tumin, A., and Theofilis, V., "Towards the foundation of a global modes concept," *6th AIAA Theoretical Fluid Mechanics Confer*, 2011, pp. 1–18.

[11]Reed, H. L., Saric, W. S., and Arnal, D., "Linear Stability Theory Applied to Boundary Layers," *Annual Review of Fluid Mechanics*, Vol. 28, No. 1, 1996, pp. 389–428.

[12]Theofilis, V., "Advances in Global Linear Instability Analysis of Nonparallel and Three-Dimensional Flows," *Progress in Aerospace Sciences*, Vol. 39, No. 4, 2003, pp. 249–315.

[13]Arnal, D., "Boundary Layer Transition: Predictions Based on Linear Theory," *Special course on Progress in Transition Modelling*, No. R-793, AGARD, ISBN: 92-835-0742-8, 1994.

[14]Canuto, C., Hussaini, M., Quarteroni, A., and Zang, T., *Spectral Methods - Fundamentals in Single Domains*, Springer Verlag, Berlin, 2006.

[15]Trefethen, L., *Spectral Methods in MATLAB*, Society for Industrial and Applied Mathematics, 2001.

[16]Weideman, J. and Reddy, S., "A MATLAB differentiation matrix suite," *ACM Trans. Math. Softw.*, Vol. 26, No. 4, Dec. 2000, pp. 465–519.

[17]Orszag, S. A., "Accurate solution of the Orr-Sommerfeld stability equation," *Journal of Fluid Mechanic*, Vol. 50, 1971, pp. 689–703.

[18]Malik, M. R., "Numerical methods for hypersonic boundary layer stability," *Journal of Computational Physics*, Vol. 86, No. 2, 1990, pp. 376–413.

[19]Schlichting, H., Gersten, K., Krause, E., Oertel, H. J., and Mayes, C., "Boundary Layer Theory Springer," *Eigth Revised and Enlarged Edition*, 2000.

[20]Anderson, J., *Hypersonic and high temperature gas dynamics*, AIAA, 2006.

[21]White, F., *Viscous Fluid Flow*, McGraw Hill Series in Mechanical Engineering, McGraw-Hill Professional Publishing, 1991.

[22]Mack, L., "Special Course on Stability and Transition of Laminar Flow," *AGARD, Special Course of Stability and Transition of Laminar Flows*, North Atlantic Treaty Organization, ISBN: 92-835-0355-4, June 1984.

[23]Pinna, F., *Numerical study of stability of flows from low to high Mach number*, Ph.D. thesis, Università di Roma- "La Sapienza", Von Kármán Institute, Rhode-Saint-Genèse, 2012.

[24]Oliviero, N. B., *EPIC: a New and Advanced Nonlinear Parabolized Stability Equation Solver*, Ph.D. thesis, Texas A&M University, 2015.

[25]Roache, P. J., *Fundamentals of Computational Fluid Dynamics*, Hermosa Publishers, 1998.

[26]Press, W. H., Teukolsky, S. a., Vetterling, W. T., and Flannery, B. P., *Numerical Recipes in Fortran: the Art of Scientific Computing. Second Edition*, Vol. 1, 1986.

[27]Burden, R. and Faires, J., *Numerical Analysis*, Brooks/Cole, Cengage Learning, 2010.

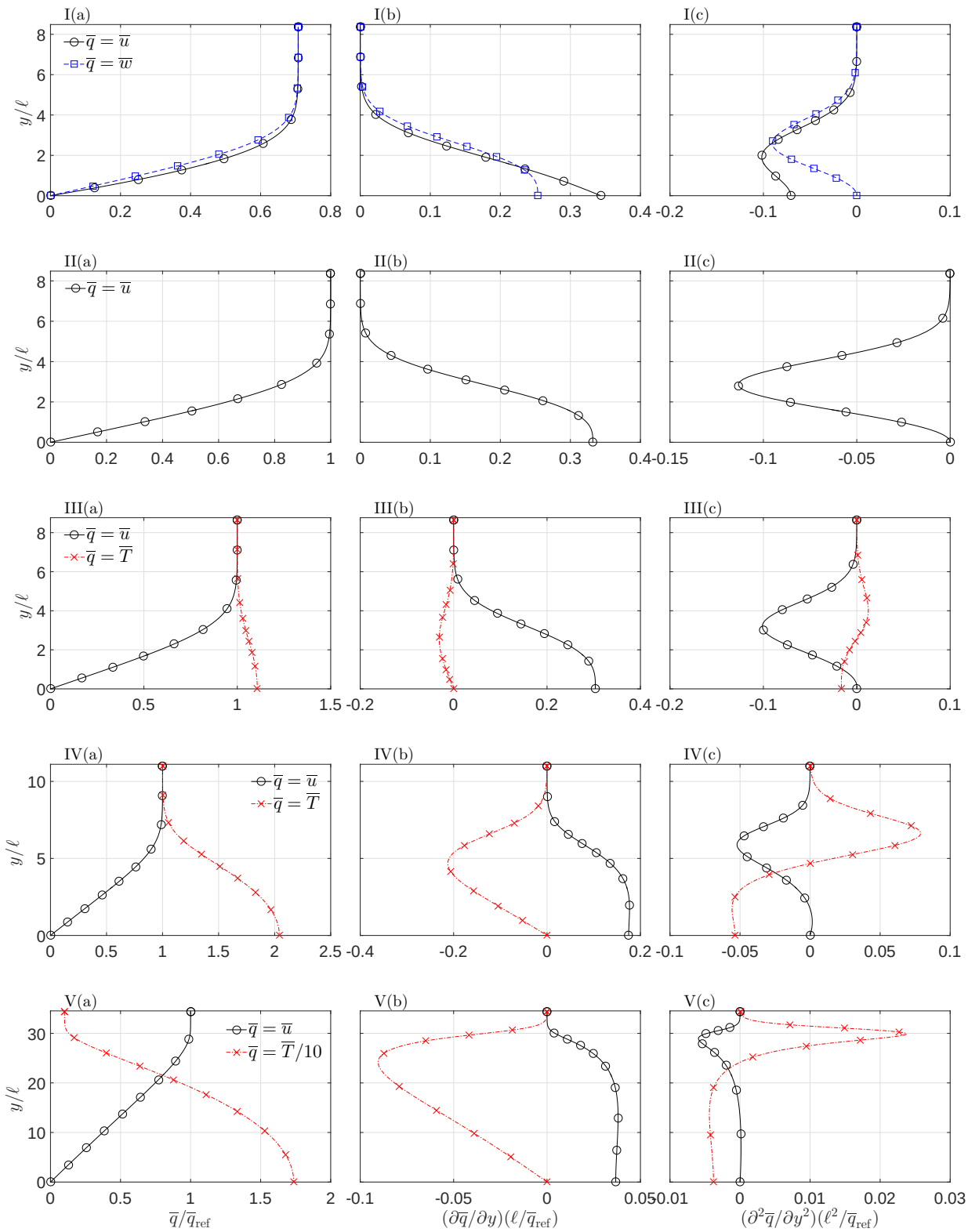

Figure 9. Boundary-layer profiles of the x- and z- velocity components (resp. black and blue, $\overline{q}_{\rm ref} = \overline{Q}_e$) and the temperature (red, $\overline{q}_{\rm ref} = \overline{T}_e$). The roman numerals correspond to those in table 4. The panel columns indicate the function value (a) and the first (b) and second (c) derivatives.

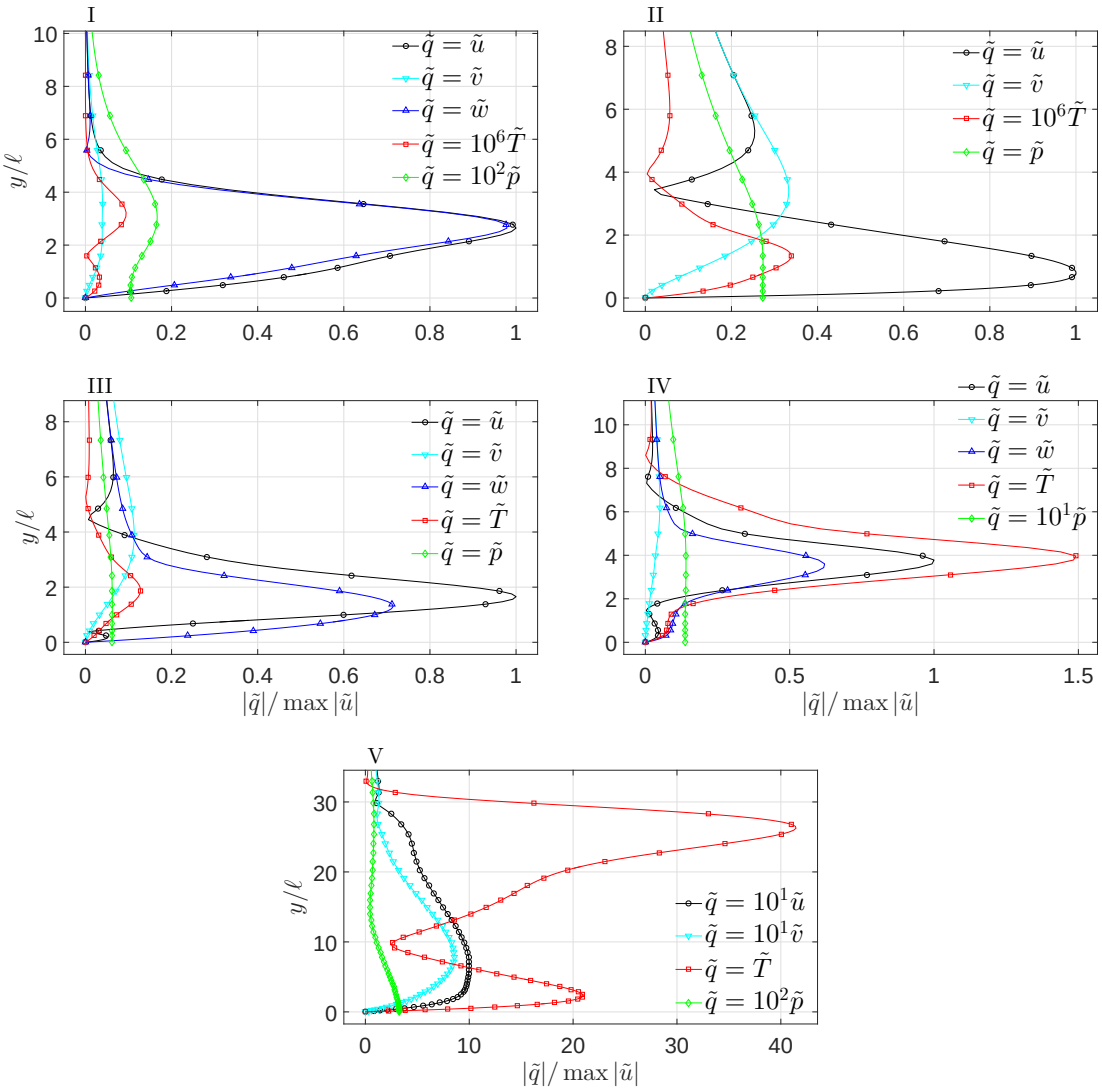

Figure 10. Eigenfunctions profiles. The roman numerals correspond to those in table 4. For case I and II, the incompressible stability solutions are indicated with the dots. The number of points $\bar{N} = 150$ for all cases except V, which required $\bar{N} = 500$.

[28]Runge, C., "Ueber die numerische Auflosung von Differentialgleichungen," *Mathematische Annalen*, Vol. 46, No. 2, 1895, pp. 167–178.

[29]Mack, L. M., "A numerical study of the temporal eigenvalue spectrum of the Blasius boundary layer," *Journal of Fluid Mechanics*, Vol. 73, No. 3, 1976, pp. 497–520.

[30]Groot, K. J., *Derivation of and Simulations with BiGlobal Stability Equations*, M.Sc. thesis, Delft University of Technology, The Netherlands, 2013.

[31]Lehoucq, R. B., Sorensen, D. C., and Yang, C., "ARPACK Users Guide: Solution of Large Scale Eigenvalue Problems by Implicitly Restarted Arnoldi Methods." 1997.

[32]Moler, C. B. and Stewart, G. W., "An algorithm for generalized matrix eigenvalue problems," *SIAM Journal on Numerical Analysis*, Vol. 10, No. 2, 1973, pp. 241–256.

[33]Kocian, T. S., *Computational Hypersonic Boundary-Layer Stability and the Validation and Verification of EPIC*, Ph.D. thesis, Texas A&M University, 2018.

[34]Arnoldi, W. E., "The principle of minimized iterations in the solution of the matrix eigenvalue problem," *Quarterly of Applied Mathematics*, Vol. 9, No. 1, 1951, pp. 1729.

[35]Herbert, T., Stuckert, G., and Lin, N., "Method for Transition Prediction in High-Speed Boundary Layers," Tech. rep., WL-TR-93-3097. Air Force Materiel Command Wright-Patterson AFB, 1993.

[36]Hermanns, M. and Hernandez, J. A., "Stable high-order finite-difference methods based on non-uniform grid point distributions," *International journal for numerical methods in fluids*, Vol. 56, No. 3, 2008, pp. 233–255.

[37]Paredes, P., Hermanns, M., Le Clainche, S., and Theofilis, V., "Order 10^4 speedup in global linear instability analysis using matrix formation," *Computer Methods in Applied Mechanics and Engineering*, Vol. 253, 2013, pp. 287–304.

[38]Paredes, P., Theofilis, V., Rodríguez, D., and Tendero, J., "The PSE-3D instability analysis methodology for flows depending strongly on two and weakly on the third spatial dimension," *6th AIAA Theoretical Fluid Mechanics Conference*, 2011, p. 3752.

[39]De Tullio, N., Paredes, P., Sandham, N. D., and Theofilis, V., "Laminarturbulent transition induced by a discrete roughness element in a supersonic boundary layer," *Journal of Fluid Mechanics*, Vol. 735, 2013, pp. 613646.

[40]Theofilis, V., "Inviscid Global Instability of Compressible Flow on an Elliptic Cone: Algorithmic Developments," Tech. Rep. F61775-00-WE069, EOARD, 2002.